Progetto S3 – Scenari di scuotimento in aree di interesse prioritario e/o strategico

Responsabili: Francesca Pacor (INGV-MI) e Marco Mucciarelli (Unibas)

TASK 1 – SCENARI DI SCUOTIMENTO

Deliverable 0: Tecniche di simulazione

A cura di
UR1 – *Francesca Pacor, Gianlorenzo Franceschina, Gabriele Ameri, Gaetano Zonno*
UR2 – *Giovanna Cultrera, Antonella Cirella, André Herrero , Ingrid Hunstad, Alessio Piatanesi, Laura Scognamiglio, Elisa Tinti*
UR10 – *Antonio Emolo, Frantisek Gallovic*

INDEX

1. SIMULATION TECHNIQUES

1.1. Stochastic methods

1.1.1. Point source stochastic method (PSSM)

The point source stochastic method (PSSM) proposed by Boore (1983, 2003), consists in a windowed random time series whose imposed spectrum matches, only on average, a specified Fourier amplitude spectrum based on seismological model of point source, path and site effects. White noise is windowed by an envelope function represented by a simple analytical expression. Then, the spectrum of the normalized transient time series is multiplied by the specified ground motion spectrum and back-transformed to the time domain.
The essence of the method is shown in figure 1.1, where the ground motion at a particular distance and site condition for magnitude 5 and 7 earthquakes are shown. The time series are produced by assuming that this motion is distributed with a random phase over a time duration related to earthquake size and propagation distance, whereas the spectraare based on a sismological model. Typically the acceleration spectrum is modelled by a spectrum with a ω–squared shape (Aki, 1967; Brune, 1970,1971; Boore 1983, 2003). The "ω–squared model" spectrum is derived for an instantaneous shear dislocation at a point. The acceleration spectrum of the shear wave at a hypocentral distance R from a given earthquake is:

$$FAS(f) = CM_0 \frac{(2\pi f)^2}{\left(1+\left(\frac{f}{f_c}\right)^2\right)} A(f) \exp(-\pi f k) \exp\left(\frac{-\pi f R}{Q(f)\beta}\right) \frac{1}{R^N}$$

By separating the spectrum of ground motion into source , path and site components, the models based on the stochastic method can be easily modified to account for specific situation.

- Source Parameters
  - M Moment magnitude
  - Δσ Stress Drop
- Path Parameters
  - N Geometrical spreading coefficient
  - Q(f) Anelastic attenuation along ray path
- Site Parameters
  - k Accounts for damping in shallow rock
  - A(f) Amplification factor for the impedance contrast from source to site

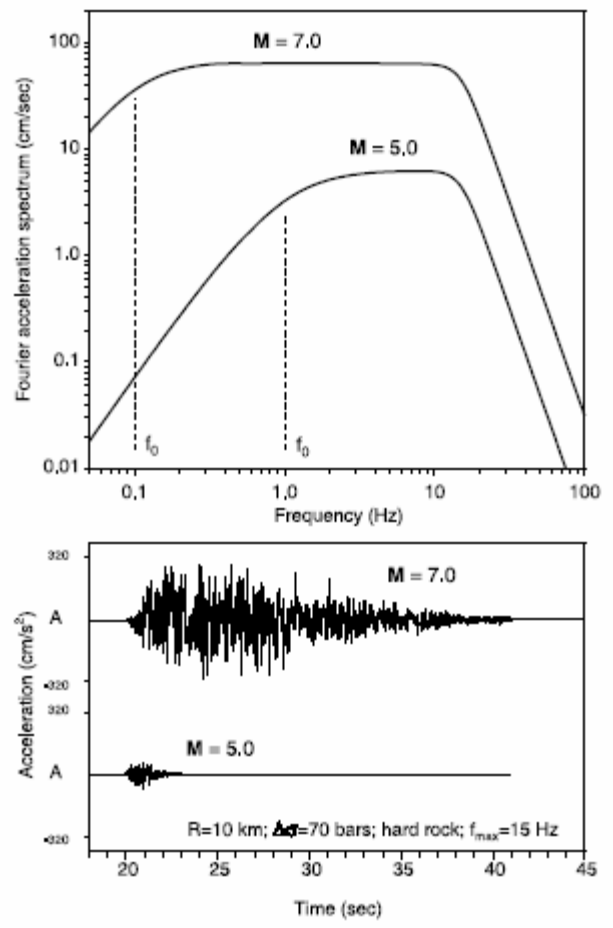

Figure 1.1 - Basis for stochastic method (from Boore 2003). Radiated energy described by the spectra in the upper part of the figure is assumed to be distributed randomly over a duration equal to the inverse of the lower corner frequency (f0). Each time series is one realization of the random process for the actual spectrum shown. When plotted on a log scale, the levels of the low-frequency part of the spectra are directly proportional to the logarithm of the seismic moment and thus to the moment magnitude. Various peak ground-motion parameters (such as response spectra, instrument response, and velocity and acceleration) can be obtained by averaging the parameters computed from each member of a suite of acceleration time series or more simply by using random vibration theory, working directly with the spectra.

1.1.2. Stochastic finite-fault simulation (Finsim)

The computer code FINSIM is a program developed by Beresnev and Atkinson [1997 and 1998], that generalizes the stochastic simulation technique proposed for point sources by Boore [1983] to the case of finite faults. The fault plane, assumed to be rectangular, is subdivided into an appropriate number of sub-faults, which are modeled as point sources characterized by an ω–squared spectrum. The sub-fault seismic moment and corner frequency are derived from the size of each cell and the number of sub-faults triggered is adjusted to reach the specified target seismic moment.

The rupture front, spreading radially from the hypocenter, triggers the sub-faults when it reaches their center and the sub-fault acceleration time histories are

propagated to the observation point using specified duration and attenuation models. A random component is included in the sub-sources trigger times to account for the complexity in the ground motion generation process. The corner frequency of the ω–squared spectrum is related to the sub-fault size by the parameter *z*, that is also linked to the maximum slip velocity.
The amplitude of sub-fault radiation is proportional to z^2. The "standard" value for the z parameter is 1.68 [Beresnev and Atkinson, 1997] but the code allows to vary its value, in order to model "unusual" fast or slow events. FINSIM can be applied to events down to Mw=4.0 in any tectonic environment, due to the flexibility in the specification of the input parameters which include models of distance-dependent sub-source duration, geometric and intrinsic Q(*f*) attenuation.
The user can also specify the slip distribution on the fault plane and two separate amplifications, in order to account for crustal amplification and local site response. If a specific slip distribution is not selected, the program will generate a random normally distributed slip whose standard deviation is equal to the slip mean.
The simulations are performed by the computer code EXSIM (Extended Finite-Fault Simulation , Motazedian and Atkinson, 2005) that is an updated version of FINSIM. The modifications introduce the new concept of a "dynamic corner frequency" that decrease with time as the rupture progresses, to model more closely the effects of finite-fault geometry on the frequency content radiated ground motions (Motazedian and Atkinson, 2005). The model has several significant advantages with respect to previous stochastic finite-fault models, including thr independence of results from subfault size, conservation of radiated energy, and the ability to have only a portion of the fault active at any time during the rupture, simulating in this way self-healing behaviour (Heaton, 1990).

1.2. Deterministic methods

1.2.1. Static displacement simulation (Okada)

We compute static displacements using a dislocation model in an elastic, homogeneous, isotropic half-space (see Okada 1985 and references therein). The fault is represented by a rectangular dislocation where slip distribution is homogeneous; a heterogeneous slip distribution can be represented as a sum of several subsources distributed on the fault plane. The source parameters of the rupture model are the fault length, width, strike and dip, the depth of the top of the fault, and the strike and dip components of the slip vector.

The mathematical representation of the Okada solution was obtained following Steketee (1958). He showed that the displacement field $u_i(x_1, x_2, x_3)$ due to a dislocation $\Delta u_j(\xi_1, \xi_2, \xi_3)$ across a surface Σ in an isotropic medium is given by:

$$u_i = \frac{1}{F}\int\int_{\Sigma} \Delta u_j \left[\lambda \delta_{jk} \frac{\partial u_i^n}{\partial \xi_n} + \mu \left(\frac{\partial u_i^j}{\partial \xi_k} + \frac{\partial u_i^k}{\partial \xi_j} \right) \right] \nu_k d\Sigma$$

where, δ_{ik} is the Kroneker delta, λ and μ are Lamè's constants, ν_k is the direction cosine of the normal to the surface element $d\Sigma$, and the Einstein summation convention applies.

u_i^j is the *i*-th component of the displacement at (x_1, x_2, x_3) due to the *j*-th direction point force of magnitude F at (ξ_1, ξ_2, ξ_3).

The Cartesian coordinate system is taken as in figure 1.2. Elastic medium occupies the region $z \le 0$ and the x axis is taken to be parallel to the strike direction of the fault. The elementary dislocations U_1, U_2 and U_3 are defined so as to correspond to strike-slip, dip-slip and tensile components of arbitrary dislocation. In Figure 1.2, each vector represents the movement of hanging-wall side block relative to foot-wall side block.

The surface displacement due to a point source located at $(0,0,-d)$ are

For strike-slip

$$u_x = -\frac{U_1}{2\pi}\left[\frac{3x^2 q}{R^5} + I_1 \sin\delta \right] \Lambda\Sigma$$

$$u_y = -\frac{U_1}{2\pi}\left[\frac{3xyq}{R^5} + I_2 \sin\delta \right] \Lambda\Sigma$$

$$u_z = -\frac{U_1}{2\pi}\left[\frac{3xdq}{R^5} + I_4 \sin\delta \right] \Lambda\Sigma$$

For dip-slip

$$u_x = -\frac{U_2}{2\pi}\left[\frac{3xpq}{R^5} + I_3 \sin\delta\cos\delta \right] \Lambda\Sigma$$

$$u_y = -\frac{U_2}{2\pi}\left[\frac{3ypq}{R^5} + I_1 \sin\delta\cos\delta \right] \Lambda\Sigma$$

$$u_z = -\frac{U_2}{2\pi}\left[\frac{3dpq}{R^5} + I_5 \sin\delta\cos\delta \right] \Lambda\Sigma$$

where

$$I_1 = \frac{\mu}{\lambda+\mu} y \left[\frac{1}{R(R+d)^2} - x^2 \frac{3R+d}{R^3(R+d)^3} \right]$$

$$I_2 = \frac{\mu}{\lambda+\mu} x \left[\frac{1}{R(R+d)^2} - y^2 \frac{3R+d}{R^3(R+d)^3} \right]$$

$$I_3 = \frac{\mu}{\lambda+\mu}\left[\frac{x}{R^3} \right] - I_2$$

$$I_4 = \frac{\mu}{\lambda+\mu}\left[-xy\frac{2R+d}{R^3(R+d)^2}\right]$$

$$I_5 = \frac{\mu}{\lambda+\mu}\left[\frac{1}{R(R+d)} - x^2\frac{2R+d}{R^3(R+d)^2}\right]$$

and

$$p = y\cos\delta + d\sin\delta$$
$$q = y\sin\delta - d\cos\delta$$
$$R^2 = x^2 + y^2 + d^2 = x^2 + p^2 + q^2 .$$

These equations can easily be extended to a finite rectangular fault with length L and width W by taking $x-\chi'$, $y-\eta'\cos\delta$ and $d-\eta'\sin\delta$ in place of x, y and d.

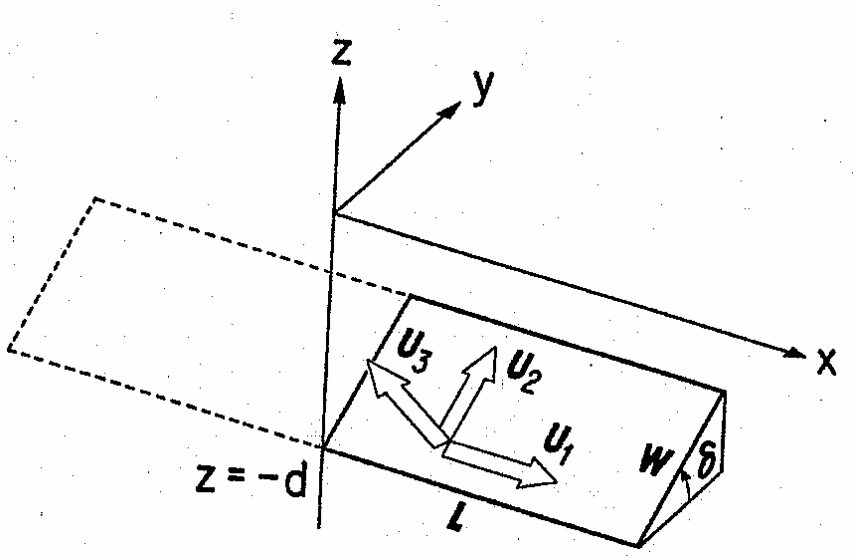

Figure 1.2 - Geometry of the source model for Okada technique.

1.2.2. Finite element and finite difference numerical method (Compsyn)

The most general deterministic techniques for simulating ground motion consist in solving the elastic equations using the finite element and finite difference numerical methods which accommodate arbitrary 3-dimensional Earth structures. These methods converge to exact solution at wavelengths longer than the associated numerical grid dimensions, but suffer from extreme computational expense when source and observer are separated by more than a few wavelength (Day, 2001). More economical solutions are obtained by modelling the Earth with layers of constant elastic parameters.

One of these methods is the COMPSYN code (Spudich and Xu, 2002), based on the finite element and finite difference numerical methods to calculate synthetic ground

motion seismograms for hypothetical fault ruptures occurring on faults of spatial finite extent.
The wave propagation through a layered velocity model is simulated by computing the Green's functions with the Discrete Wavenumber / Finite Element (DWFE) method of Olson et al. (1984). The application assumes that the Earth model is defined as a 1D layered elastic medium, therefore anelastic attenuation is not considered in the computation. This technique allows to calculate the complete response of an arbitrarily complicated Earth structure, so that all P and S waves, surface wave, leaky modes, and near-field terms are included in the synthetics seismograms. However, the code is inefficient for a simple Earth structure consisting of a few homogeneous layers but it is computationally efficient for complicated structures compared to 3-dimensional codes.
DWFE method combines the separable solutions of the elastic equations for the horizontal dependence of the seismic wavefield, with the finite element and finite difference numerical solutions for the vertical and time dependence, respectively. Its main characteristics are:

- the numerical procedure requires an artificial boundary condition at given depth; this depth is made sufficiently large so as to produce no unwanted arrivals in the time window of interest;
- the vertical grid spacing in DWFE only depends on the maximum frequency of interest (or horizontal wavenumber), and not on the vertical complexity of the model;
- although faster than other comparable finite element methods, the cost of computation increases as the cube of the number of wavelength separating source and observer, making DWFE a low-frequency method.

Once calculated the Green's functions for one selected velocity model the code allows the simulation of many hypothetical rupture models in a relativelly minimal time. The kinematics source description consists on specifying some parameters as the rupture velocity, the rise time, the slip model and the seismic moment.

COMPSYN uses a crudely adaptive integration technique (Spudich and Archuleta, 1987) to evaluate the representation theorem integrals over fault surface. The density of sample points on the fault is proportional to frequency. This integration method is more accurate than others that use explicit calculation of Green's functions and the calculation is equally accurate for waves having different phase velocity (i.e. S waves and surface waves), so it is optimally efficient at every frequency.

The operative scheme of COMPSYN is illustrated in Figure 1.3.

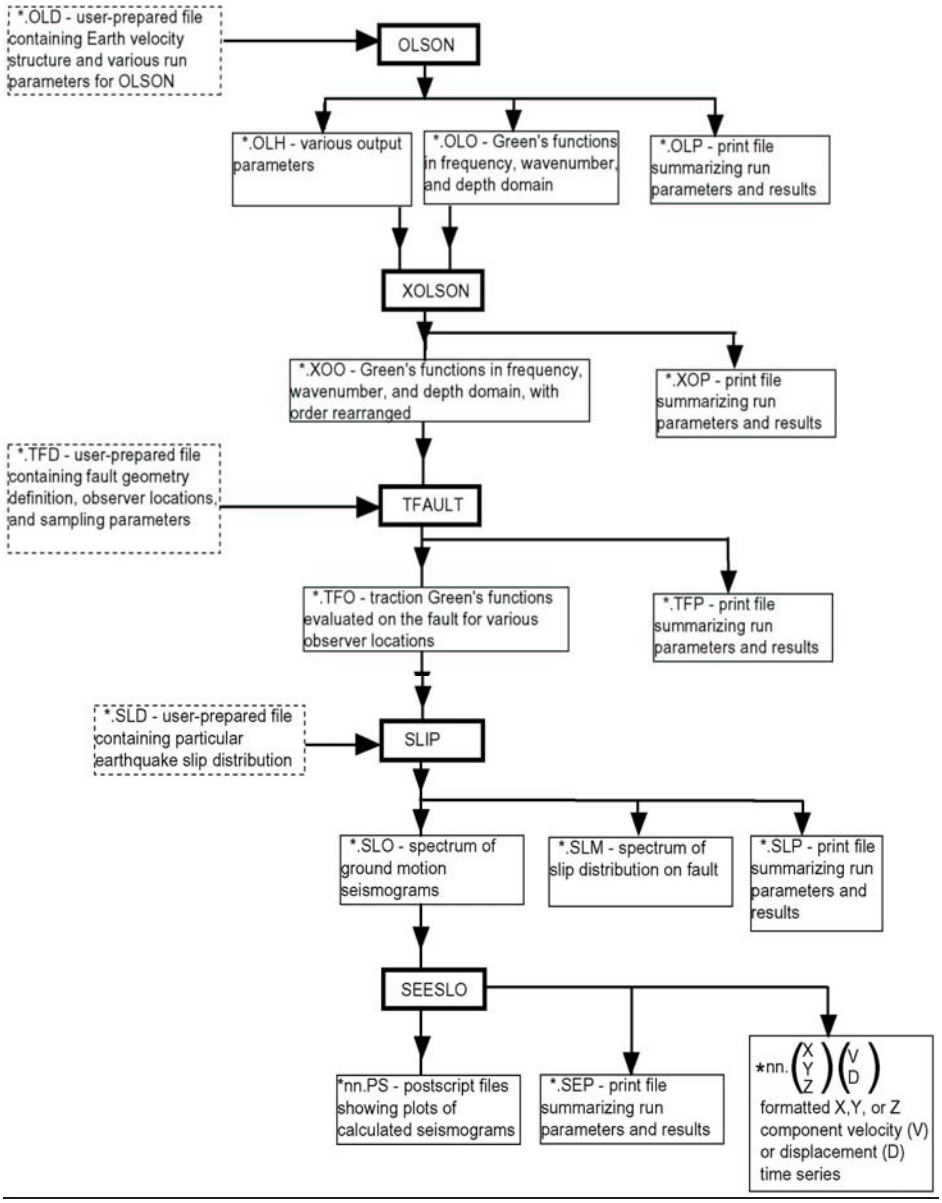

Figure 1.3 - Operative scheme of COMPSYN

1.3. Hybrid methods

1.3.1. Deterministic-stochastic method (DSM)

The DSM method (Pacor et al., 2005) is based on a modification of the point source stochastic method (PSSM) of Boore (1983) by including the effects of rupture propagation along a finite fault. The synthesis of any time series can be summarized in a four step procedure (Figure 1.4):
Step1: an acceleration envelope radiated from an extended fault is generated through isochron theory (Spudich and Frazer, 1984) assuming a simple kinematic rupture process;
Step2: a time series of Gaussian white noise is windowed with the deterministic envelope, which is smoothed and normalized so that the integral of the squared envelope is unity;
Step3: the windowed noise time series is transformed into the frequency domain and multiplied with a point-source-like amplitude spectrum. The parameters of the reference spectrum, i. e. corner frequency, distance from the fault and radiation pattern, are evaluated through the kinematic model to capture the finite-fault effects;
Step4: transformation back to the time domain. For each random noise realization a time series is obtained, but it is only the mean of the individual spectra for a number of simulations that will match the target spectrum.
The envelope contains the main features related to the directivity effects: it controls the shape and the duration of the simulated accelerograms at a given site describing how the wave-field radiated from a finite fault ultimately arrives at the site. The kinematic of the source is specified by the position of the nucleation point on a rectangular fault plane, from which the rupture propagates radially outward with a given rupture velocity. A slip distribution on the fault can also be introduced.
The generation of synthetic envelopes is based on the identification of the locus of points on the fault for which the emission of seismic radiation is characterized by the same travel time to the site of interest. These loci are called isochrones and depend on both the time of rupture of each point of the fault (unique for all sites) and the travel time from the ruptured point to the site (it varies from site to site and depends on the propagation medium). The isochrones define the time scale to sum the response of the medium to the rupture of each point of the fault (i.e. Green's functions). The Green's functions are calculated as simply Dirac delta functions scaled by geometrical spreading (1/R) and radiation pattern ($R_{\theta\phi}$). The envelope form is mainly controlled by the isochrones distribution; the slip and the radiation pattern modulate this basic shape, changing significantly some portion of the envelope.
The frequency content and the amplitude of the synthetic accelerograms are controlled by the reference spectrum $S(f)$:

$$S(f)=C\,A(f)\,D(f)\,T(f) \qquad (1)$$

where A(f) is the source term, D(f) is the attenuation term, T(f) is the site term.
C is a constant depending on the propagation medium:

$$C = \frac{R_{\theta\phi} F V}{4\pi\rho\beta^3 R}$$

where $R\theta\phi$ represents an average value for the radiation pattern, F is a free-surface amplification factor usually set to 2, V is a factor to account for partitioning of energy into horizontal components, ρ is the average density, β the average shear wave velocity, and R the geometrical spreading factor.
The radiation pattern and the distance between site and source depend on the extended source and are evaluated computing an average on the fault. Two different definitions are implemented: the first involves a spatial average (over the fault) at each isochron time, followed by a temporal average which is weighted by the envelope function itself (global average); the second represents the parameter averaged over the reduced fault area associated with the maximum pulse of energy arriving at site (local average).
The source spectrum $A(f)$ is assumed to have an omega-square shape, parameterized by the apparent corner frequency, f_a, instead of standard corner frequency f_c. The apparent corner frequency varies from site to site. For each receiver, it is computed by the isochron theory as the inverse of the apparent duration of rupture, T_a, as perceived by the receiver. This approach makes the corner frequency independent on the seismic moment and stress drop, as the duration is a function of the fault dimensions, nucleation point position and rupture velocity. In this way, the high frequency directivity effects are introduced in the source spectrum.

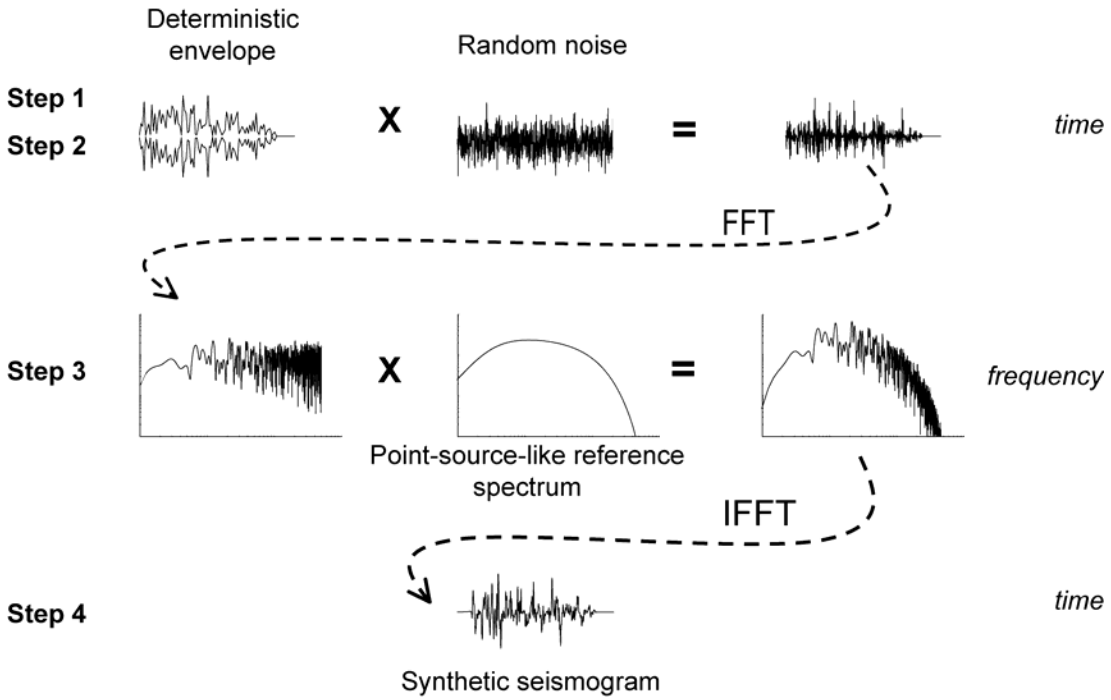

Figure 1.4 – Scheme of DSM method: white noise windowed with the deterministic envelope (steps 1 and 2); FFT multiplied with a point-source-like amplitude spectrum (step 3); IFFT (step 4).

1.3.2. hybrid k*-squared source modeling technique (HIC)*

A new modeling method for strong ground motion simulations has been developed, so called hybrid *k*-squared source modeling technique (hereinafter, HIC). For this technique, the rupture process is decomposed into slipping on the individual overlapping subsources of various sizes, distributed randomly on the fault plane. The hybrid approach combines 1) the integral approach at low frequencies, based on the representation theorem and the *k*-squared slip distribution composed by the subsources, and 2) the composite approach at high frequencies, based on the summation of ground motion contributions from the subsources. Let us emphasize that the same set of subsources is used for both the frequency ranges.
Scaling properties of the subsources are the same as used by Zeng et al. (1994). Their number-size distribution obeys a power law with fractal dimension D=2 and their mean slips are proportional to their dimensions (so-called constant stress-drop scaling). The subsource's scaling implies (Andrews, 1980) that the subsources compose a *k*-squared slip distribution.
Concerning the numerical implementation, we first build a subsource database, which includes the subsources' positions on the fault, their dimensions, mean slips (and consequently seismic moments) and corner frequencies. Subsource dimensions are taken as integer fractions of the fault's length L and width W, i.e. the subsource length is $l=L/n$ and its width is $w=W/n$. Let us call the integer n the subsource level. The number of all the subsources at levels $\leq n$ (i.e. of size L/n x W/n and larger) is considered to be n^2. More specifically, the number of subsources $N(n)$ at level n is $N(n)=n^2-(n-1)^2=2n-1$. At each level the subsources are assumed to be identical in dimensions, mean slip and corner frequency, and their position is random (and, therefore, subjected to variations in certain applications).
The mean slip for subsources at level n is given by $\Delta u(n)=c_u/n$ (obtained from the constant stress-drop assumption). We get the constant of proportionality c_u, assumed to be independent of n, by matching the seismic moment of the whole earthquake to the sum of the moments of all the subsources considered in the calculation, i.e. up to certain n_{max}.
The corner frequency f_c of the subsources at level n is considered to be proportional to n, $f_c=c_f n$. The inverse of the constant of proportionality c_f is comparable to the duration of the whole earthquake. Since f_c controls the high-frequency spectral level of the synthetics, c_f can be adjusted by comparing the synthetic PGAs or PGVs with the local attenuation relation and/or with observed time histories.
Let us describe the assumed time evolution of the rupture. At large scales, the subsources act so that the faulting is equivalent to the classical integral *k*-squared model. At low scales, the subsources behave chaotically in such a way that their radiated wave field appears effectively to be isotropic. To simulate this, for strong motion synthesis we use two methods, the integral and the composite, each for a different frequency range. Their application is controlled by two bounding frequencies f_1 and f_2 with $f_1<f_2$.
Concerning the low-frequency range (up to f_2), the computation is performed according to the representation theorem. We discretize the fault densely enough to evaluate the integral correctly up to frequency f_2. The static slip at a point is given by

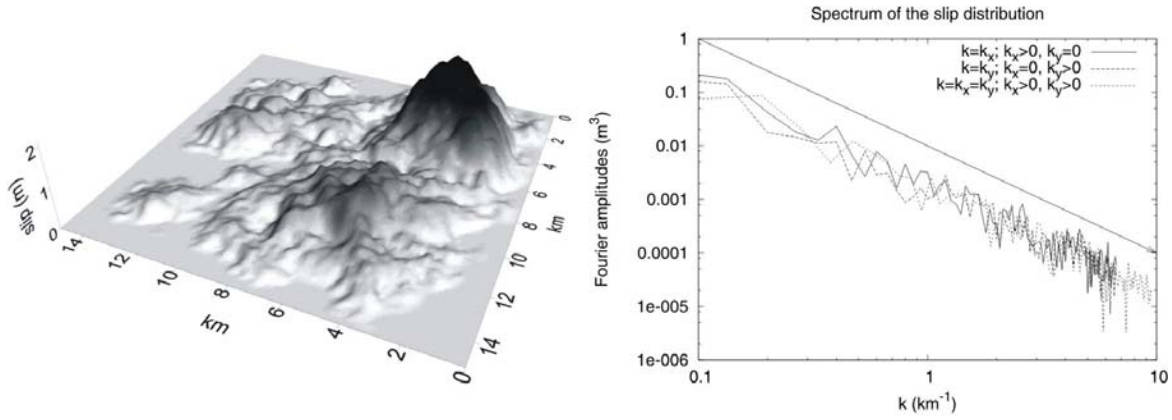

Figure 1.5 - Left: an example of slip distribution constructed from a subsource database. Note that level *n*=1 is neglected. It would correspond to a slip patch over the whole fault, which is, however, not observed in slip inversions of medium-to-large sized earthquakes. Right: three cross-sections of the spatial amplitude Fourier spectrum of the slip distribution (left). The solid line indicates the *k*-squared decay.

the sum of the static slips of all the subsources from the database that contain the point (assuming a *k*-squared slip distribution at each individual subsource). An example of the slip distribution constructed in this way is shown in Fig. 1.5. The rupture time is given by the distance of the point from the nucleation point assuming constant rupture velocity v_r. The slip velocity function is assumed to be Brune's pulse with constant rise time τ.

In the high-frequency range (above f_1), the subsources from the database are treated as individual point sources with Brune's source time function. Their seismic moments and corner frequencies are obtained directly from the database. The rupture time is given by the time the rupture needs to reach the subsource's center (assuming the same constant velocity v_r as for the integral approach). Due to the random subsource positions, the wave-field contributions sum incoherently.

The computed synthetics are crossover combined between f_1 and f_2 in the Fourier domain by weighted averaging of the real and imaginary parts of the spectrum.

In order to synthesize the final strong ground motions at a given receiver, one has to calculate Green's functions to involve effects due to the wave propagation phenomena. Generally, any method can be employed, even different for each of the two frequency ranges. We utilize just one method for both ranges. For simple 1D structure models, the source modeling method is combined with the discrete wavenumber method (Bouchon, 1981), yielding full-wavefield Green's functions.

The modeling method is explained in more detail in Gallovic and Brokeshova (2006), has been applied to the modeling of the 1999 Athens earthquake and of the 1997 Kagoshima earthquake.

2. THE IRPINIA EARTHQUAKE

The 1980 Irpinia Earthquake is a complex event that involves at least three distinct ruptures starting in a time span of approximately 40 sec. The main event (0s) was followed by a rupture episode after about 20s and one after 40s. 23 analogic accelerograms were recorded during the events, 8 of them were within the 50km from the hypocenter.
This earthquake was widely studied and a complete review is published on Special issue on the meeting "IRPINIA 10 ANNI DOPO" (Annals of Geophysics, Vol XXXVI, n. 1, April 1993).
The source models considered in this research are the Bernard and Zollo (1989) model and the Valensise et al. (1989) that are briefly summarized

2.1. Source Models from literature

2.1.1. Bernard and Zollo(1989; B&Z89) rupture model

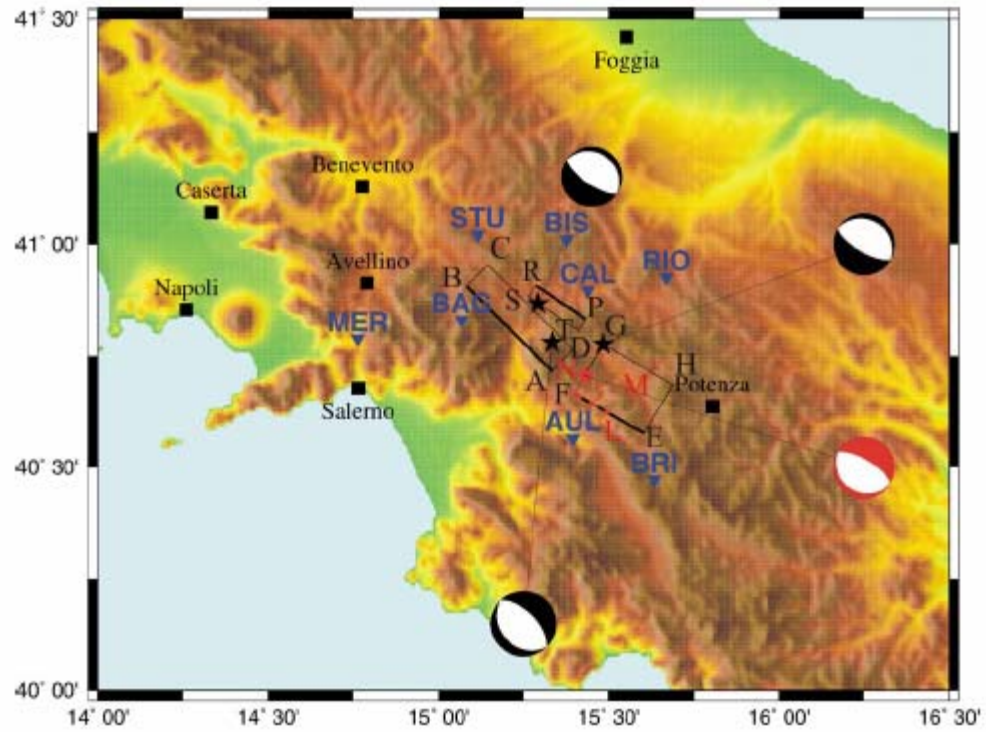

Figure 2.1 – Geometric representation of the considered fault models.

Bernard and Zollo, (1989; B&Z89) based their fault model principally on:

a) a detailed analysis of near-source recordings of the Irpinia earthquake,
b) the analysis of the geodetic measurement of surface deformation than that performed by Westaway and Jackson (1987).

The detailed analysis of principal arrivals in the near-source records allowed the authors to define a faulting scenario consistent with the timing of the main episodes

of rupture during the earthquake. This reconstruction is not trivial because of the lack of an absolute time scale for the strong motion records. The geodetic data were used in a forward modelling study to determine plausible slip values on the main fault and the "20 s" fault. As in the Westaway and Jackson study, the authors proposed a dynamic description of the rupture process and furthermore, wereable to assign values for the velocity of rupture propagation. The main results are:

a) The "20 s" event is located on a deeply buried shallow dipping fault; the authors argue that the surficial faulting in the immediate vicinity is actually associated with steeply dipping secondary faults.
b) The "40 s" fault plane is antithetic to the main rupture fault plane. This conclusion is based on inferences from the geodetic measurements, the strong motion recording at Calitri, and geological evidence for the existence of a graben structure NE of the main rupture area.
c) The final rupture model consists of 3 main faults. The authors mention the possibility of rupture occurring on a fourth fault located to the NW of the main rupture and for which the data are insufficient to clearly characterize.

Table 2.1 - Faults parameters from literature models (B&Z89, V&al89).

	0 sec from B&Z89	**20 sec** from B&Z89	**40 sec** from B&Z89	**20 sec** from V&al89
Strike (°)	315	300	124	300
Dip (°)	60	20	70	70
Rake (°)	-90	-90	-90	-90
Leght (km)	35	20	15	10
Width (km)	15	15	10	15
Top depth (km)	2.2	10	2.2	2.2
Seismic moment (Nm)	2.0 (or 1.3) 10^{19}	4.0 10^{18}	3.0 10^{18}	1.4 10^{18}
Epicenter location (long. – lat.)	15.3336 E 40.7804 N	15.4841 E 40.7766 N	15.2931 E 40.8681 N	15.4306 E 40.7067 N

2.1.2. Valensise et al. (1989; V&al89) rupture model

The other study to be considered is that of Valensise et al. (1989). These authors presented a model for the Irpinia earthquake developed from a multidisciplinary interpretation of different data set. Specifically, their model is a synthesis of information obtained from:

a) a study of the focal mechanism using the CMT inversion of long period records,
b) a study of the spatial extent of faulting from the relocalization of aftershocks in a 3-D propagation medium,
c) a study of the dynamic behaviour of the main rupture based on the forward modelling of the near-source horizontal velocity records,

d) a study to identify the fault segments involved in the rupture process, and the associated coseismic slips, based on a detailed geological mapping of their superficial expression (fault scarps) and forward modelling of geodetic data,
e) a review of previous research results which are classified by the type of data used.

The proposed fault model is similar to that of Bernard and Zollo (1989) in that the "40 s" event is located on a fault plane antithetic to the main rupture, while the "20 s" event is located on a steeply dipping fault plane which approximately coincides in position with the SE extension of the main event fault plane of Westaway and Jackson (1989).

2.2. Source and propagation model adopted in this study

The fault geometries adopted in this study (see Table 2.2) are those retrieved by Bernard and Zollo (1989) and the depth of the 20-sec fault was inferred from Valensise et al. (1989) (see Chapter 2.1 for details).

Table 2.2 – Source models

	0 sec	20 sec	40 sec
Strike (°)	315	300	124
Dip (°)	60	20	70
Rake (°)	-90	-90	-90
Leght (km)	35	20	15
Width (km)	15	15	10
Top depth (km)	2.2	5	2.2
Seismic moment (Nm)	$2.0\ 10^{19}$	$4.0\ 10^{18}$	$3.0\ 10^{18}$

For the main event we modeled the rupture scenario (rupture velocity and slip distribution) as proposed in Cocco and Pacor (1993). Directivity effects due to SE-NW rupture propagation along the 0s fault are predicted from this model.
On the other two faults, we used final slip distributions computed from the k-squared slip model of Herrero and Bernard (1994) and Gallovic and Brokešová (2004) with one asperity and hypocenters as shown in Figure 2.2. From these faulting style directivity effects are expected in NW-SE direction.

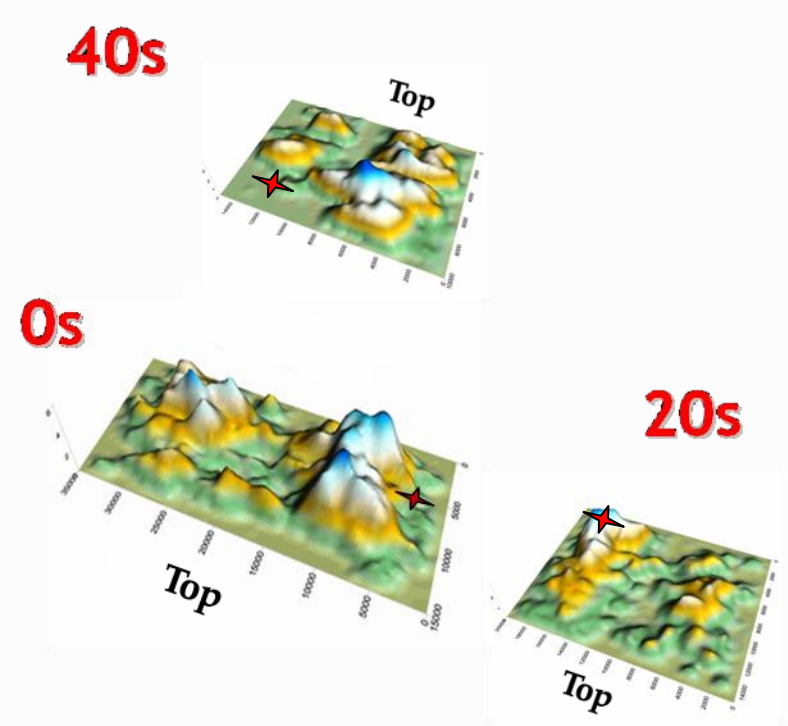

Figure 2.2 – K² slip model adopted in the simulations

The crustal velocity model has been proposed by Improta (personal communication, 2005) and it has loosely based on the Amato and Selvaggi (1993) work. It has however to be noted that the depth of the Apula platform in the area is strongly variable (Improta et al., 2003).

Table 2.3 – Crustal velocity model

depth (km)	Vp (km/s)	Vs=Vp/1.81	rho (g/cm3)	Qp	Qs	Comments
0	3.5	1.93	2.3	200	100	
2	4.5	2.49	2.5	300	150	
4	5.7	3.15	2.6	500	200	Apula platform
10	6.5	3.59	2.7	750	250	
25	7.5	4.14	2.9	900	300	
35	8.1	4.48	3.2	1200	400	Moho

2.3. Accelerometric Data

Eight accelerometric stations recorded the event in the near source area. These stations, managed by Enel (National Electric Company) were equiped by SMA-1 accelerometric sensorsIn Table 2.4 are summarized location, site condition, distance ($R_{J\&B}$) from the "0s" fault and peak acceleration values for each station. The waveforms recorded at each station are shown in Chapter 3 from figure 3.1.1 to figure 3.6.2.

Table 2.4 – Accelerometric stations (see figure 2.1).

Code	Locality	LonE	LatN	Site	Fault Distance (km)	PGA(cm/s^2)
AUL	Auletta	15.3950	40.5561	stiff soil	18.6	60.8
BAG	Bagnoli_Irpino	15.0681	40.8308	rock	6.8	164
BIS	Bisaccia	15.3758	41.0097	stiff soil with high attenuation at f >5Hz	18	98.9
BRI	Brienza	15.6344	40.4719	sediments (?)	37.2	208
CAL	Calitri	15.4386	40.8983	stiff soil on landslide	13	179
MER	Mercato_San_Severino	14.7628	40.7894	soft soil	28.7	142
RIO	Rionero_in_Vulture	15.6689	40.9272	soft soil (alluvial deposits)	29.2	103
STU	Sturno	15.1150	41.0208	fractured rock	3.8	307

2.4. Preliminary modeling

We used two different techniques to check the reliability of the complex fault models for the Irpinia earthquake. In particular, the top depth for the 20s faults was chosen using a trial and error process to minimize the misfit with data.

2.4.1. Envelope simulation

The large wavelength characteristics of the adopted source models for the 0s, 20s and 40s sub-events were calibrated by comparing the *acceleration envelopes*, computed by the DSM technique (Chapter 1.3.1), with the recorded accelerograms filtered in the [0.5 – 2.5]Hz frequency band. The results in figure 2.3 show that, despite of the very simple kinematic source models assumed, we obtained synthetic envelopes that fit the direct S-wave arrivals of the recorded ground accelerations at the selected sites.
For instance, the **STR** station is dominated by a strong pulse due to the rupture propagation along the 0s fault toward the site. Similarly, the strong amplitude

recorded at **BRI** station is radiated by the 20s event.

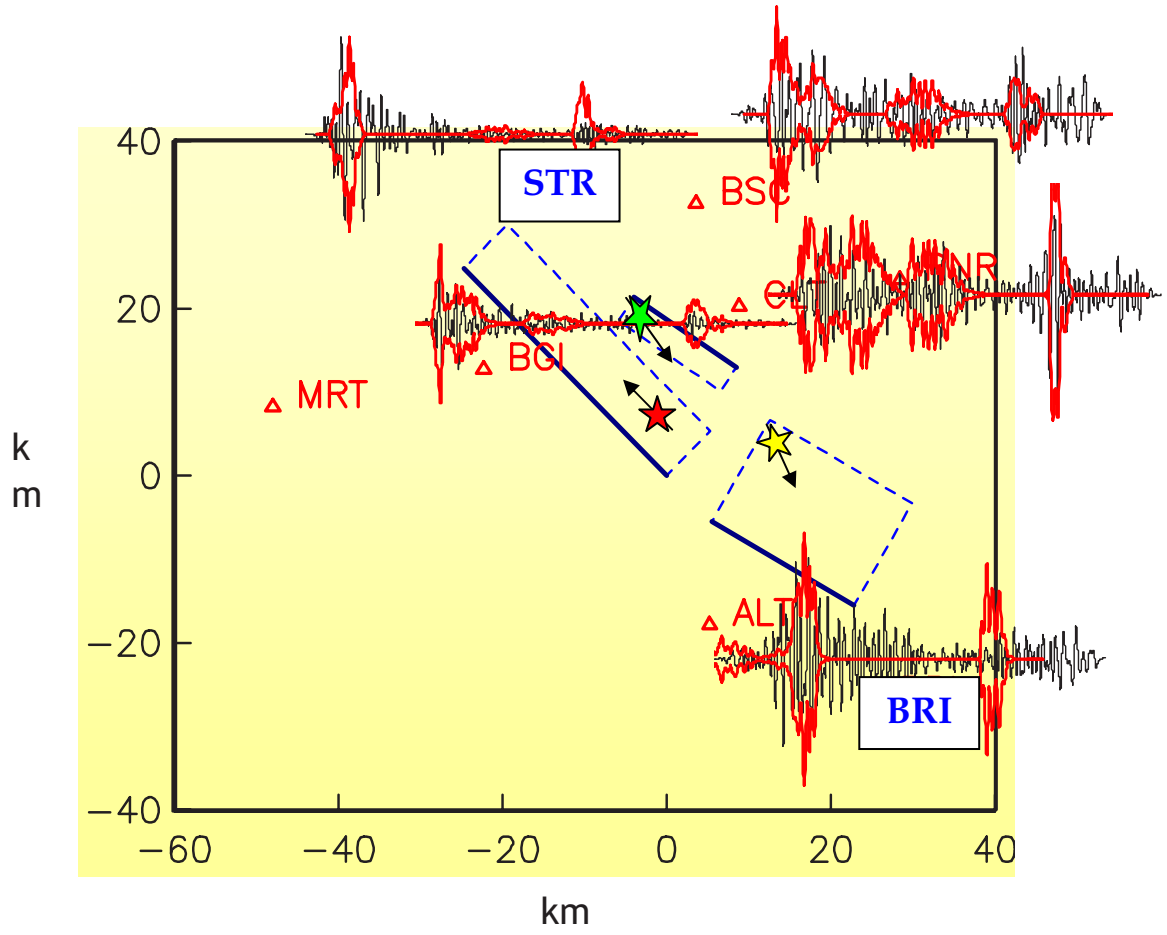

Figure 2.3 – Comparison between simulated envelopes and recorded accelerograms for different test sites.

2.4.2. Stochastic simulation

A finite-fault stochastic approach was applied in the 1980 Irpinia earthquake simulation using the code EXSIM (Motazedian and Atkinson, 2005) that is an updated version of FINSIM (see chapter 1.1.2). A preliminary analysis is performed considering the three faults (herein named 0, 20 and 40 sec) at the same time to simulate both the near source and the regional ground motion, in terms of time series and response spectra, taking in account source and propagation parameters available coming from previous papers.

The computed time series of each stations is compared with the recorded ones to see what the relation with the subsequent ruptures on nearby faults. The computed shaking scenarios are compared with the acceleration records in terms of response spectra (5 % damping) for the 8 stations located in the Irpinia epicenter area. We don't use at the moment the possibility of EXSIM to generate the impulsive long-period velocity pulses that can be caused by forward directivity of the source (Motazedian and Atkinson, 2005) with an analytical approach. The preliminary

results are shown in figure 2.4 and 2.5 but the calibration and validation of all parameters of the models are not yet completed.
We have used the dynamic corner frequency model with a stress drop of 100 bars, a value of Q equal to 85 and with the option 90% of the fault actively slipping at any time in the rupture. In the evaluation of the results we have to take into account that actually we have used given slip distribution with a grid of about 2 km x 2 km for all three faults (0, 20 and 40 sec).

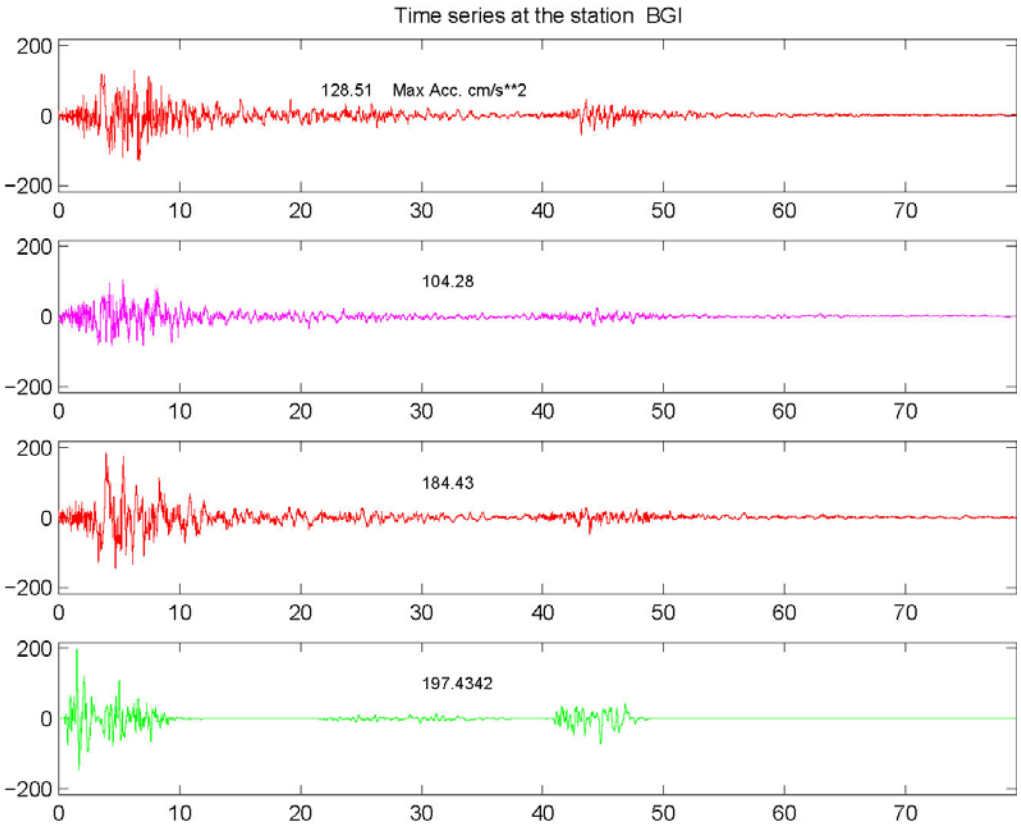

Figure 2.4- Comparison of observed time history (red) with the simulated at the BGI station.

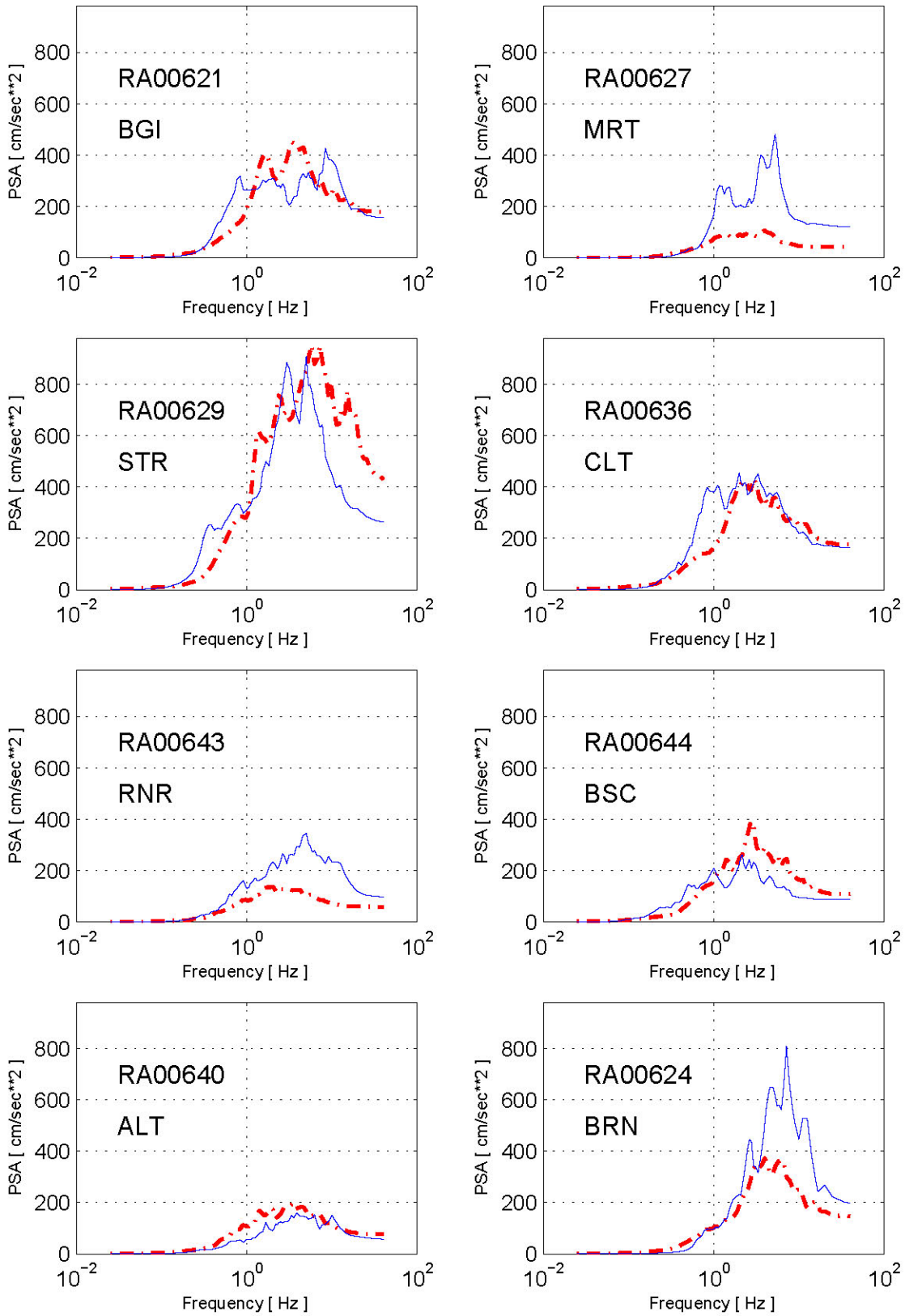

Figure 2.5 - Comparison of the observed 5% damped pseudo-acceleration response spectra (blue lines) with the spectra simulated (dotted red lines) for the three faults (0, 20 and 40 sec) at the stations (BGI, MRT, STR, CLT, RNR, BSC, ALT and BRN). The geometric mean of two observed components are shown by solid lines (blue). The station BGI (Bagnoli Irpino) is located on hard rock and the fitting of the response spectra seems good.

3. COMPARISON OF SIMULATION TECHNIQUES

The simulation techniques described in Chapter 1 have been used to model the Irpinia 1980 earthquake (0-second event). We used the forward source model and the velocity crustal profile as in Chapter 2.2, and we performed simulation at the sites where accelerometric stations recorded the earthquake. Site effects were not taken into account.
The following paragraphs report the comparison between the synthetics from different methods and with recorded data from the Irpinia 1980 earthquake.

First of all, we compared the synthetics for each site both in time and frequency domains. The comparison has been performed in the frequency band of validity of each technique (see Chapter 1 for details), due to the computational limits or accuracy requirements related to the chosen simulation parameters: f>0.1 Hz for DSM, f<5 Hz for Compsyn, f<10 Hz for HIC and f=0 Hz for Okada. Hereinafter are the main comments on the results as shown in Figures 3.*x*.1 (where *x*=1,2,3,4,5,6):

1. The velocity time series generated by
2. Compsyn and HIC are almost equivalent and they are controlled by the low frequency content (f< 1Hz) for all sites. Differences on the HIC simulations can be caused by i) the anelastic attenuation that is not accounted in Compsyn, ii) at frequencies higher than 0.5 Hz (up to 2 Hz) the low-frequency synthetics starts being cross-over filtered with the high-frequency part so that it affects the seismograms in some way. Moreover, the Compsyn synthetics have lower amplitude for frequency larger than 1 Hz because the size of heterogeneity of the source model and of the propagation velocity structure used for this study could not radiate high frequency motion.

The high amplitude of HIC simulation at STU (Figure 3.6.1a) is due to the forward source directivity for this site that is pronounced by a low frequency two-sided velocity pulse.
2. DSM technique simulates only direct S-waves and this is evident from the shorter duration of time series. The lower velocity amplitude of the time series is due to the lack of low frequency content (f<~0.3 Hz).
3. The high frequencies amplitudes of ground motion computed with HIC and DSM are quite similar for BAG (Figure 3.1.1a) and MER (Figure 3.4.1a). Sites BIS (Figure 3.2.1a), CAL (Figure 3.3.1a) and RIO (Figure 3.5.1a) show lower amplitude for DSM simulations: this is basically due to the dependence of DSM technique on directivity (BIS, CAL and RIO sites are non-directive) and to the different Green's function computation (full-wavefield in HIC method and direct S-waves in DSM).
The very high amplitude of DSM simulation at STU (Figure 3.6.1a) is due to the strong directivity effect which increases the apparent corner frequency.
4. The static displacement computed by the Okada technique for homogeneous propagation medium fits very well the final displacement of Compsyn for all the sites (Figures 3.*x*.1b). Moreover, we verified that the use of a stratified velocity model does not affect the results.

We then compared the synthetics with the accelerometric data recorded at the 6

accelerometric stations that triggered on the P-wave arrival (Table 3.1).

Table 3.1 - . Location and geological characteristics of sites where simulation are performed.

Code	Locality	LonE (deg)	LatN (deg)	Site condition
BAG	Bagnoli_Irpino	15.07	40.83	rock
BIS	Bisaccia	15.38	41.00	Stiff soil with high attenuation at f >5Hz
CAL	Calitri	15.44	40.90	stiff soil on landslide
MER	Mercato San Severino	14.76	40.79	soft soil
RIO	Rionero in Vulture	15.67	40.93	soft soil (alluvial deposits)
STU	Sturno	15.11	41.02	fractured rock

The aim of this comparison was to check if the simulations are qualitatively consistent with real data without pretending to fit them. Moreover, we did not account for site effects that are present in some of the considered sites (Table 3.1). Both synthetics and recorded data are filtered: the high-pass corner frequency is due to the instrumental filter (fmin=0.15Hz), whereas the low-pass corner frequency is constrained by the frequency limit of each technique (5 Hz for Compsyn, 10 Hz for HIC) or by the instrumental filter (25 Hz).
Figures 3.*x*.2 (where *x*=1,2,3,4,5,6) show that the agreement is quite good both in frequency and time domain, despite of the simple assumptions that has been made. The differences at **CAL** (Figures 3.3.2), **MRT** (Figures 3.4.2) and **RNR** (Figures 3.5.2) are mainly due to recognized site effects (Table 3.1).

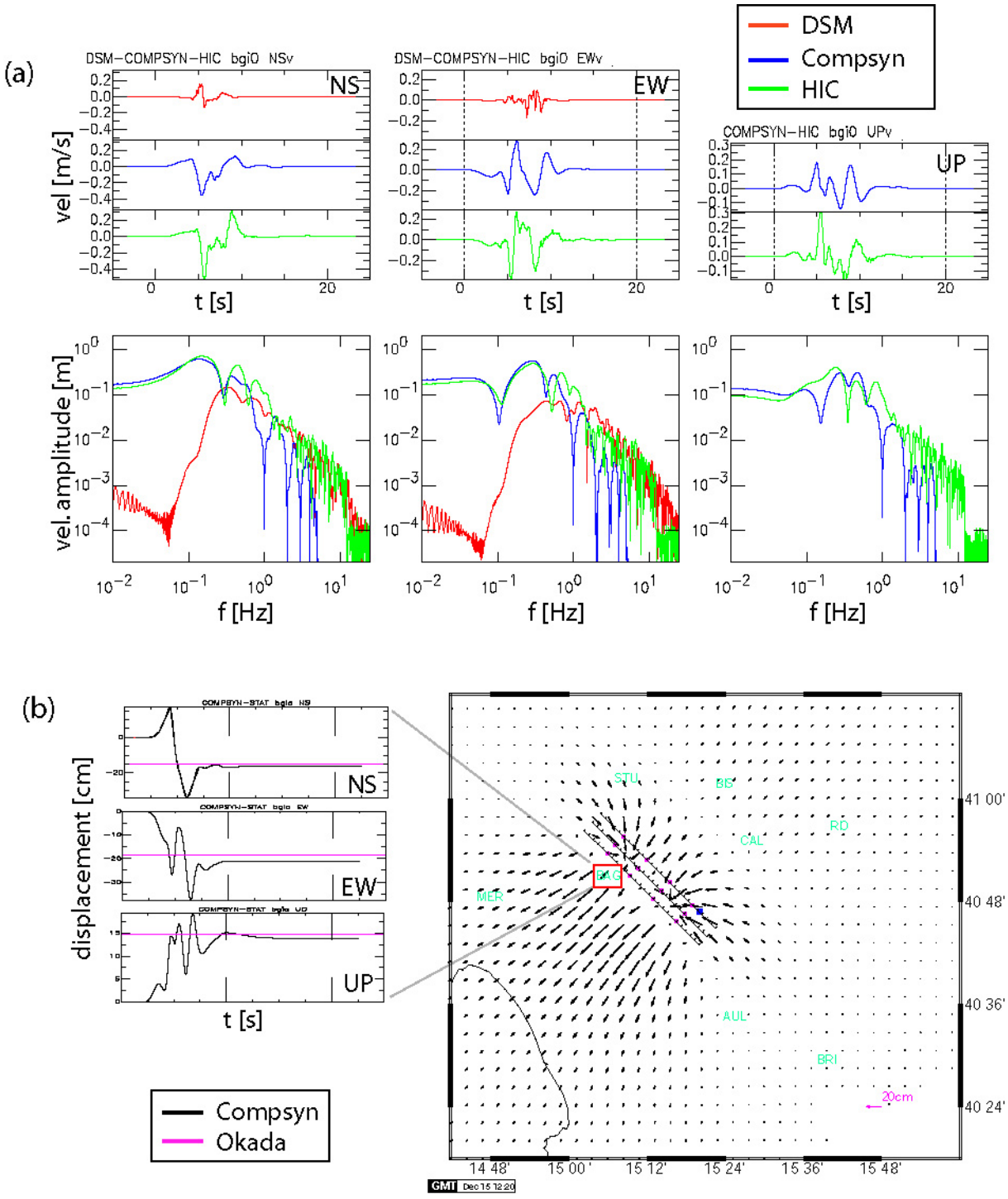

Figure 3.1.1 Comparison between synthetics from different simulation techniques (DSM, Compsyn, HIC, Okada) at Bagnoli Irpino (BAG): (a) velocity time series and Fourier amplitude (DSM, Compsyn, HIC); note that the DSM technique allows to compute the horizontal components only. (b) Displacement time series computed by Compsyn method and Okada static displacement; the arrows on the right-hand side indicate amplitude and direction of the static displacement field computed for the studied area.

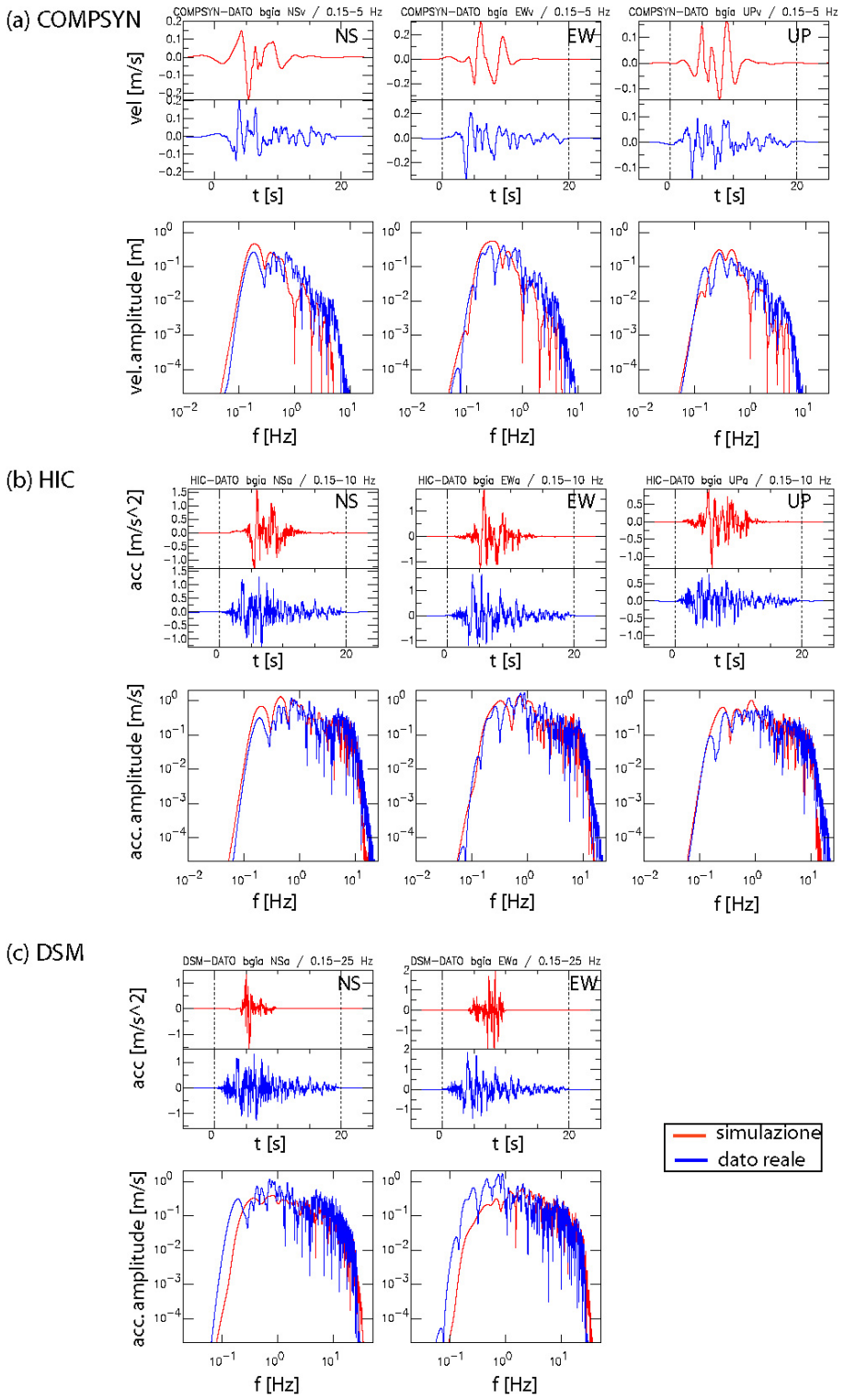

Figure 3.1.2 Comparison between synthetics and recordings (in time and frequency domain) for the 0s event of the 1980 Irpinia earthquake at BAG. We used a time window of 20 seconds to avoid the arrival from the later events: (a) Compsyn simulation and recorded velocity filtered between 0.15 and 5 Hz (NS, EW and UP components); (b) HIC simulation and recorded acceleration filtered between 0.15 and 10 Hz (NS, EW and UP components); (c) DSM simulation and recorded acceleration filtered between 0.15 and 25 Hz (NS and EW components).

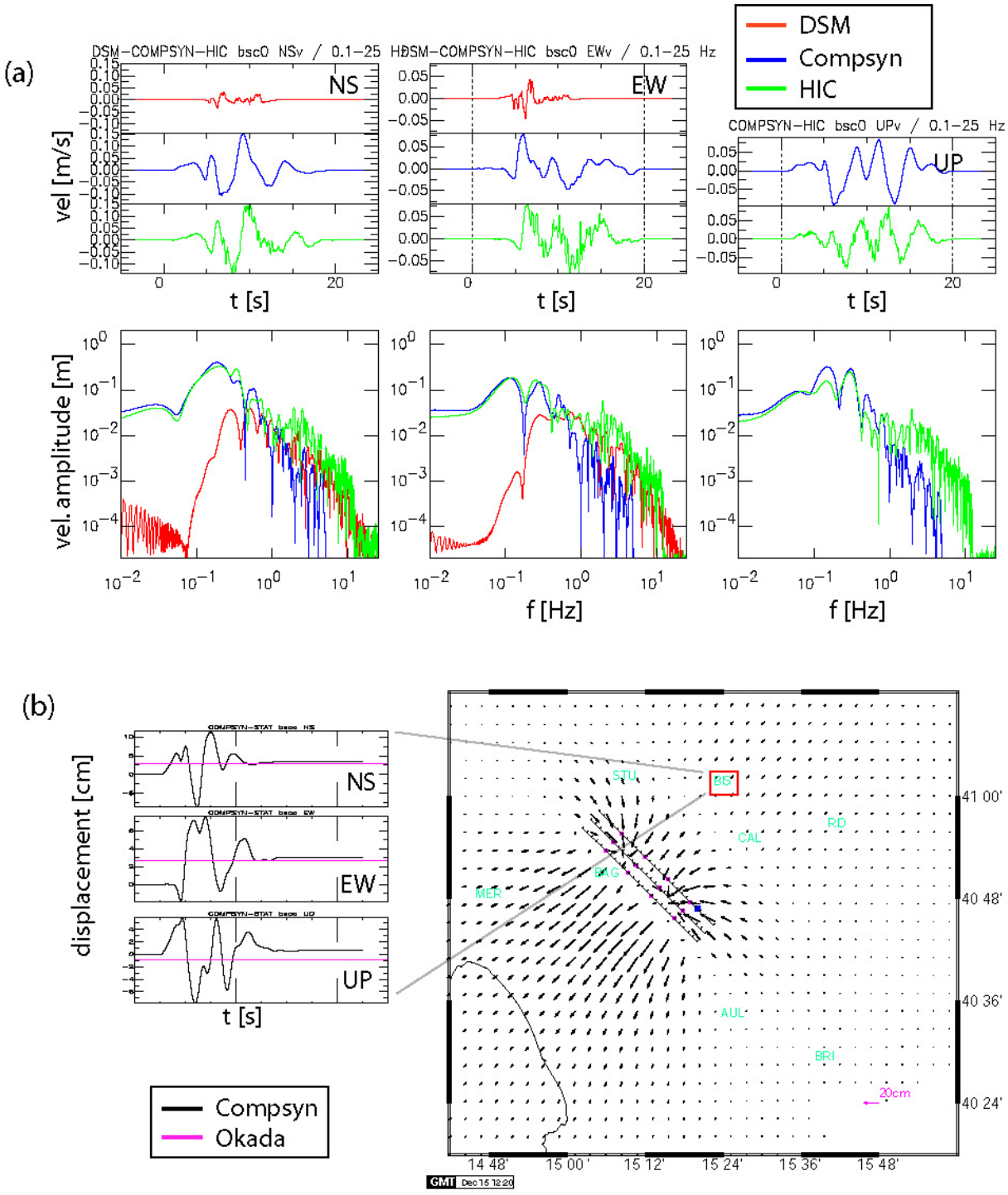

Figure 3.2.1. Same caption of Figure 3.1.1 but for Bisaccia (BIS)

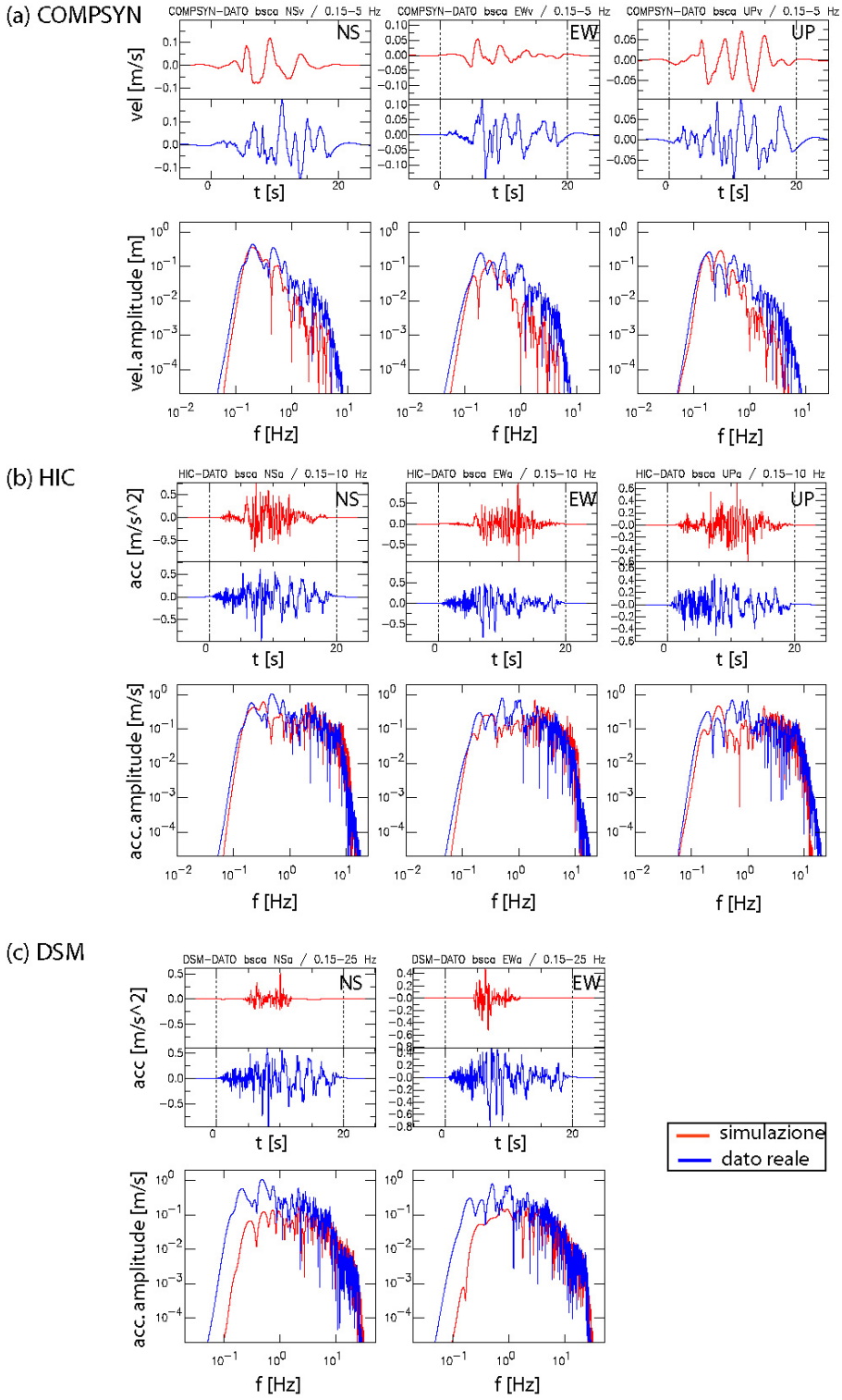

Figure 3.2.2. Same caption of Figure 3.1.2 but for BIS

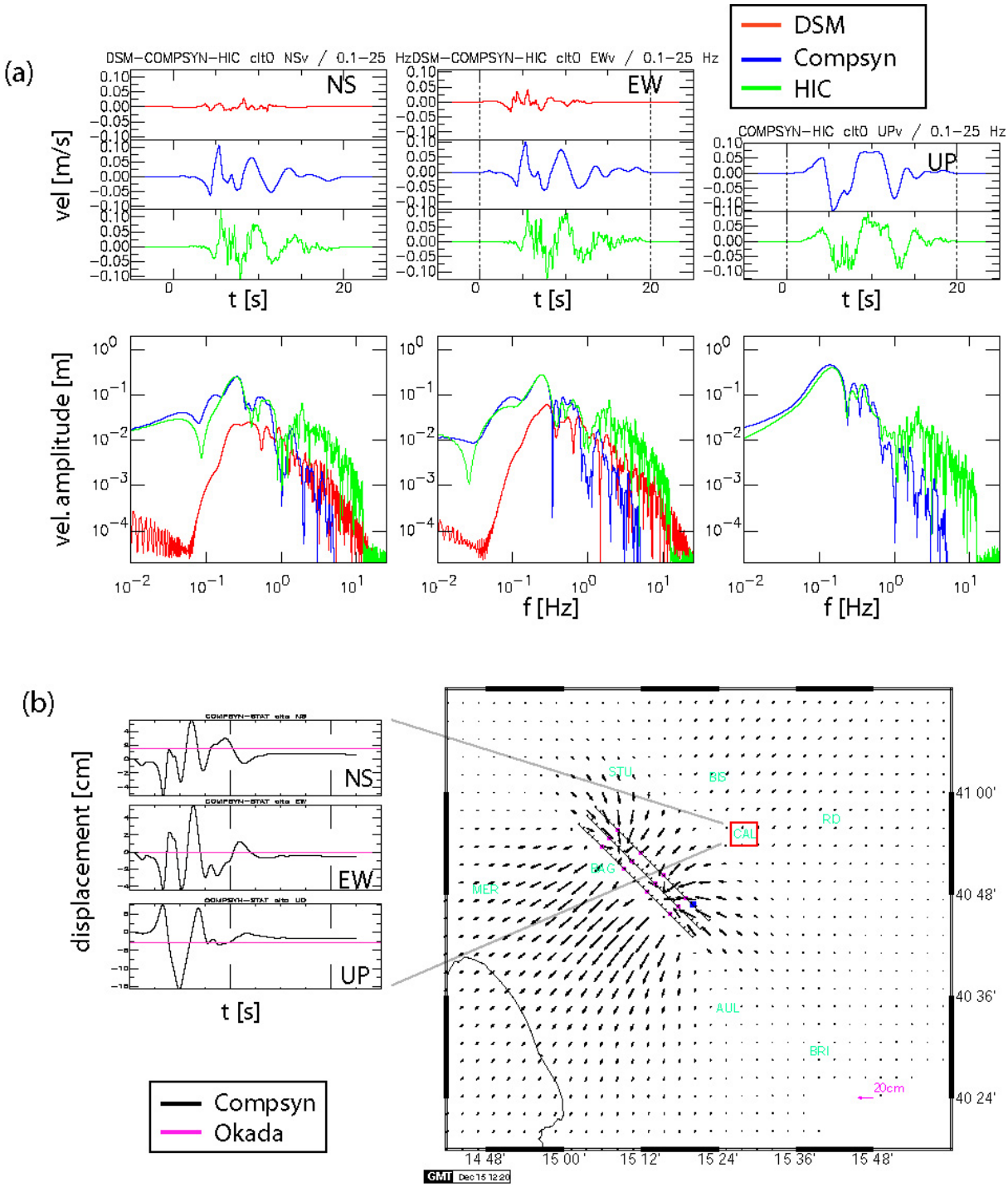

Figure 3.3.1 Same caption of Figure 3.1.1 but for Calitri (CAL)

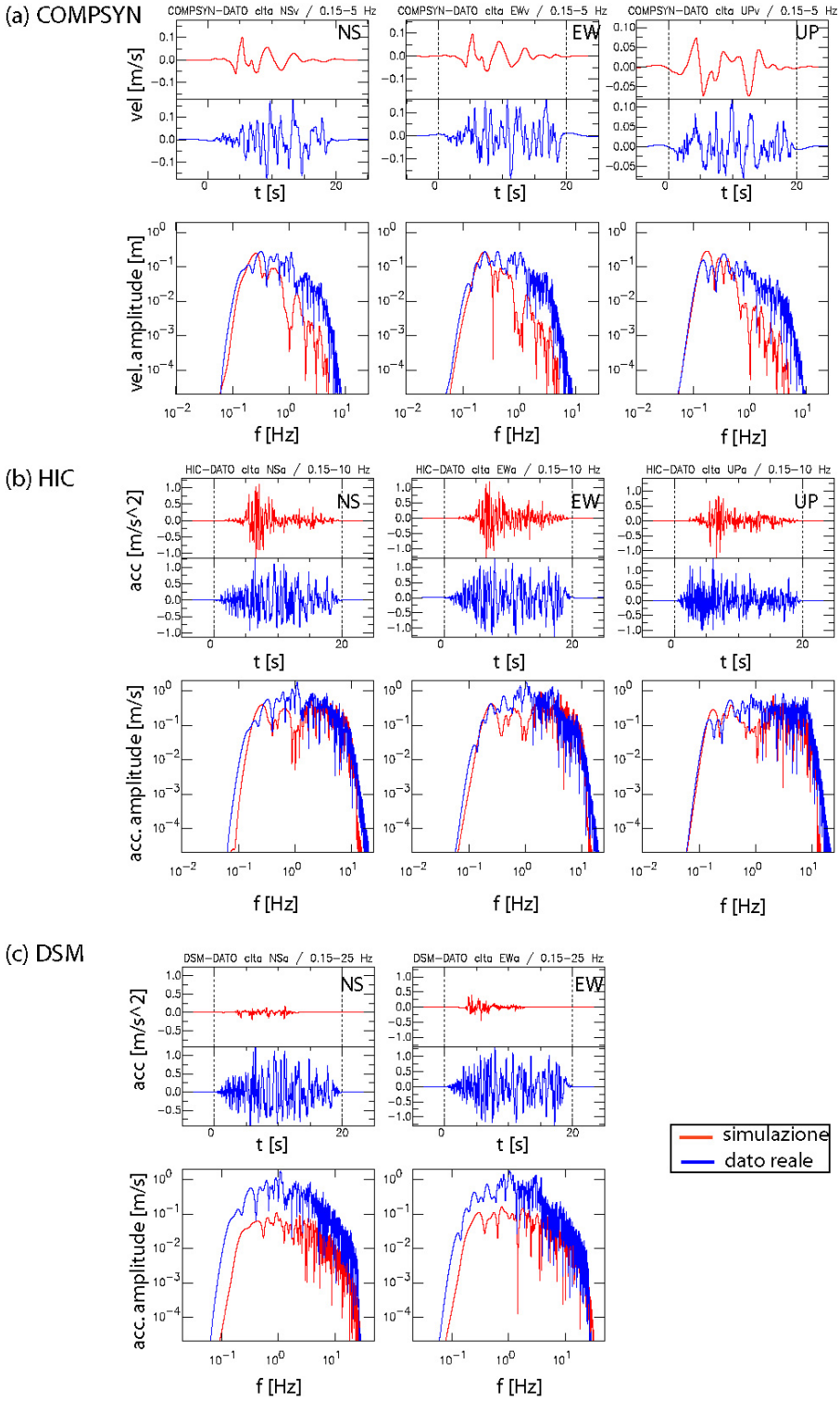

Figure 3.3.2. Same caption of Figure 3.1.2 but for CAL

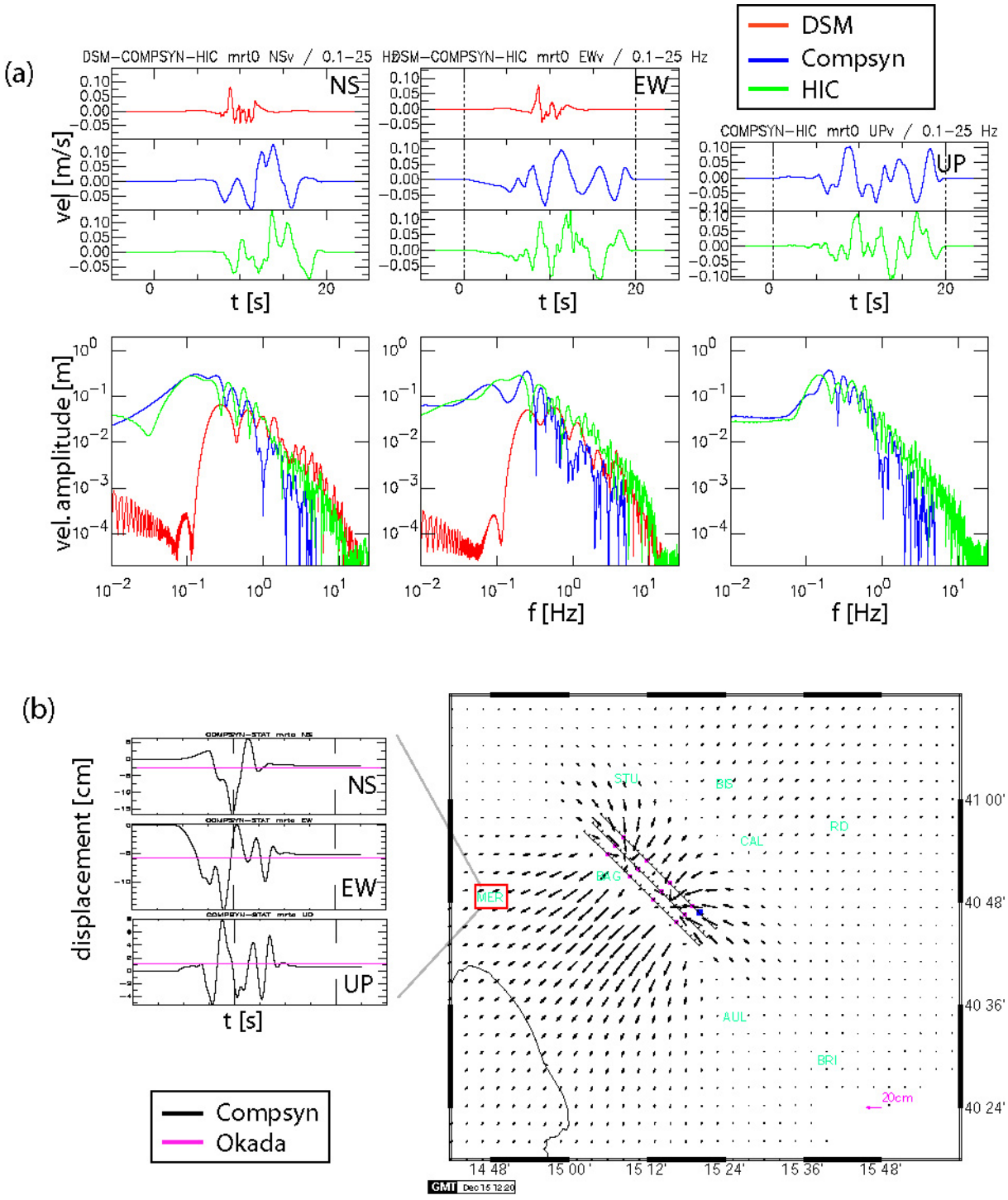

Figure 3.4.1 Same caption of Figure 3.1.1 but for Mercato San Severino (MER)

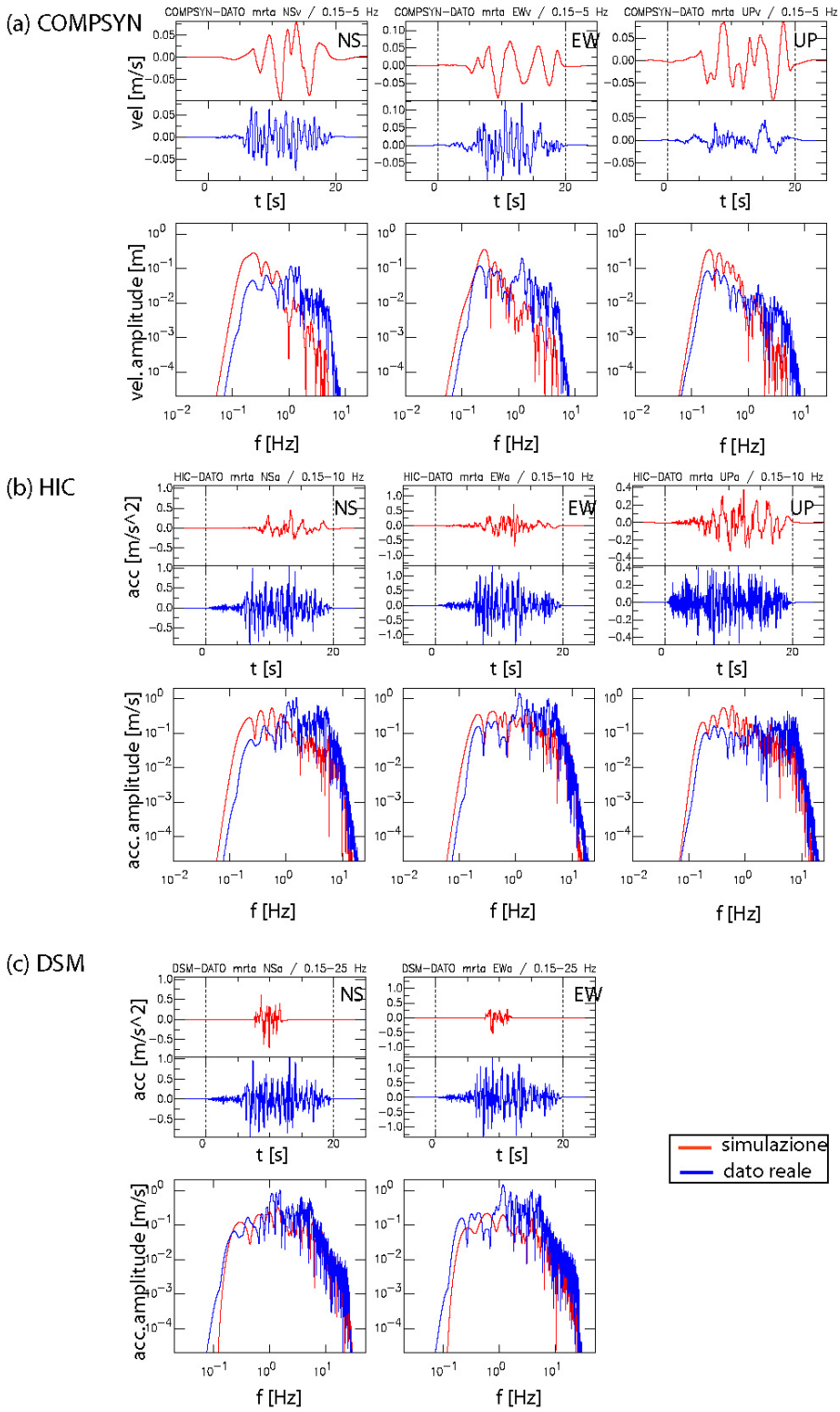

Figure 3.4.2. Same caption of Figure 3.1.2 but for MER

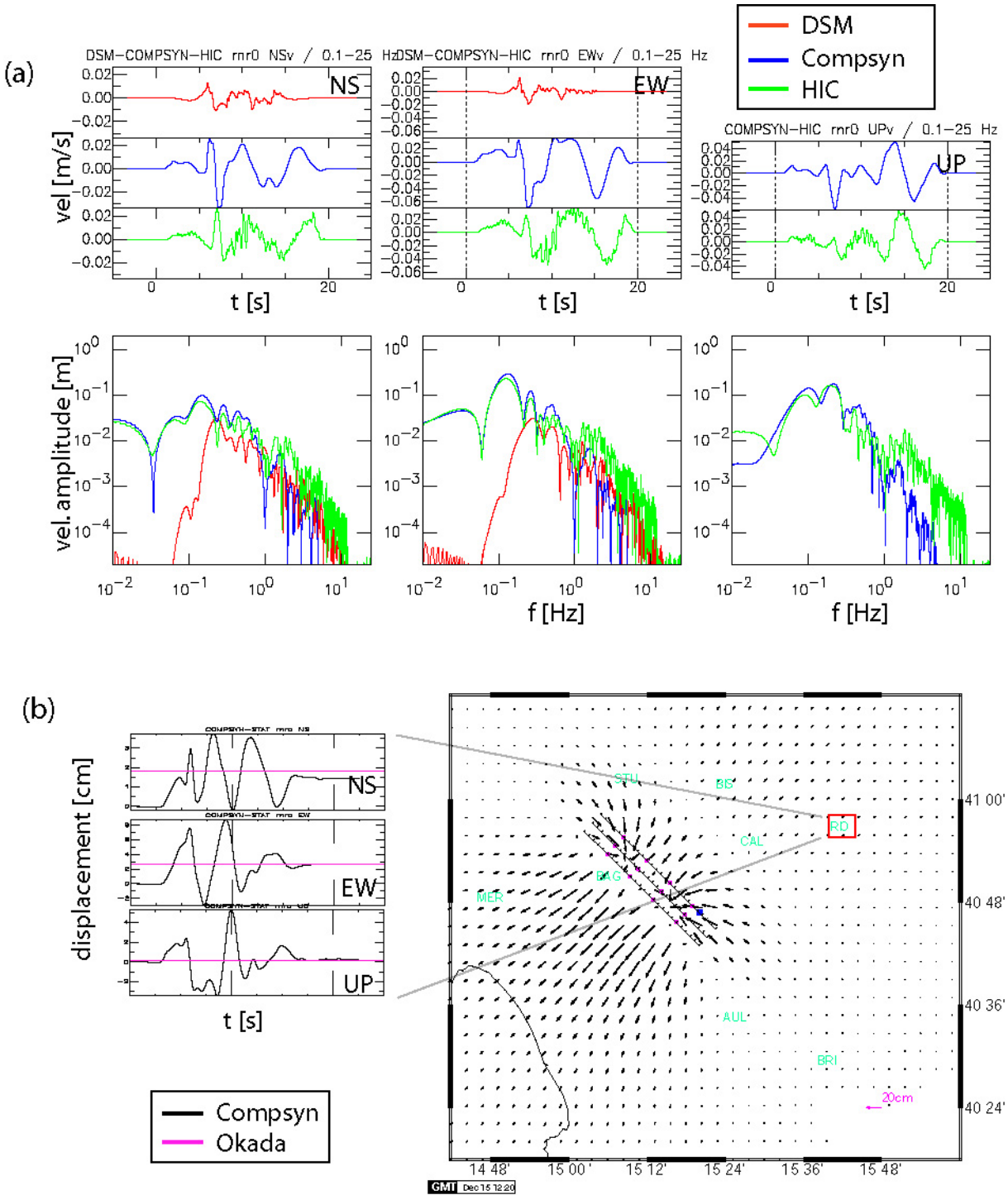

Figure 3.5.1 Same caption of Figure 3.1.1 but for Rionero in Vulture (RIO)

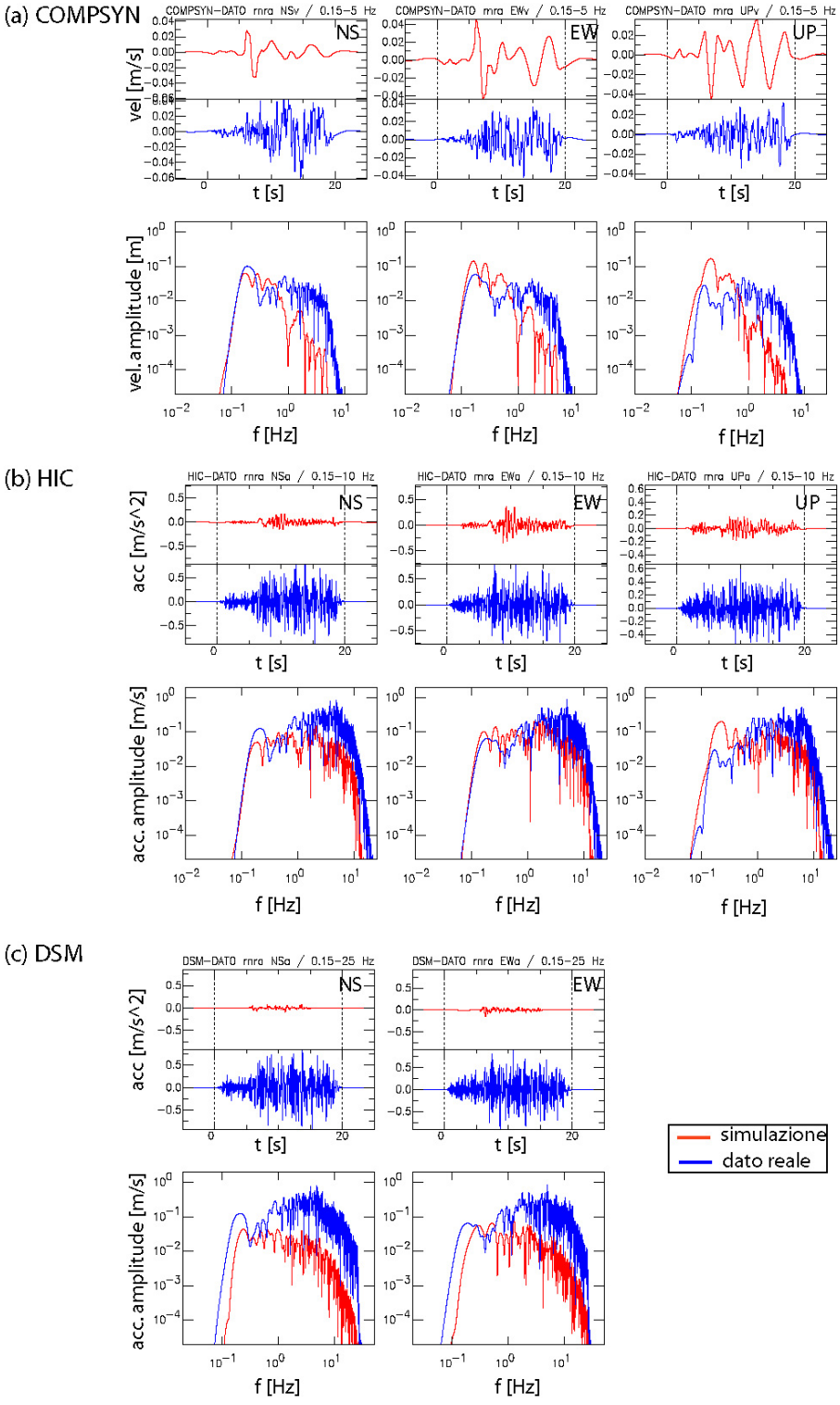

Figure 3.5.2. Same caption of Figure 3.1.2 but for RIO

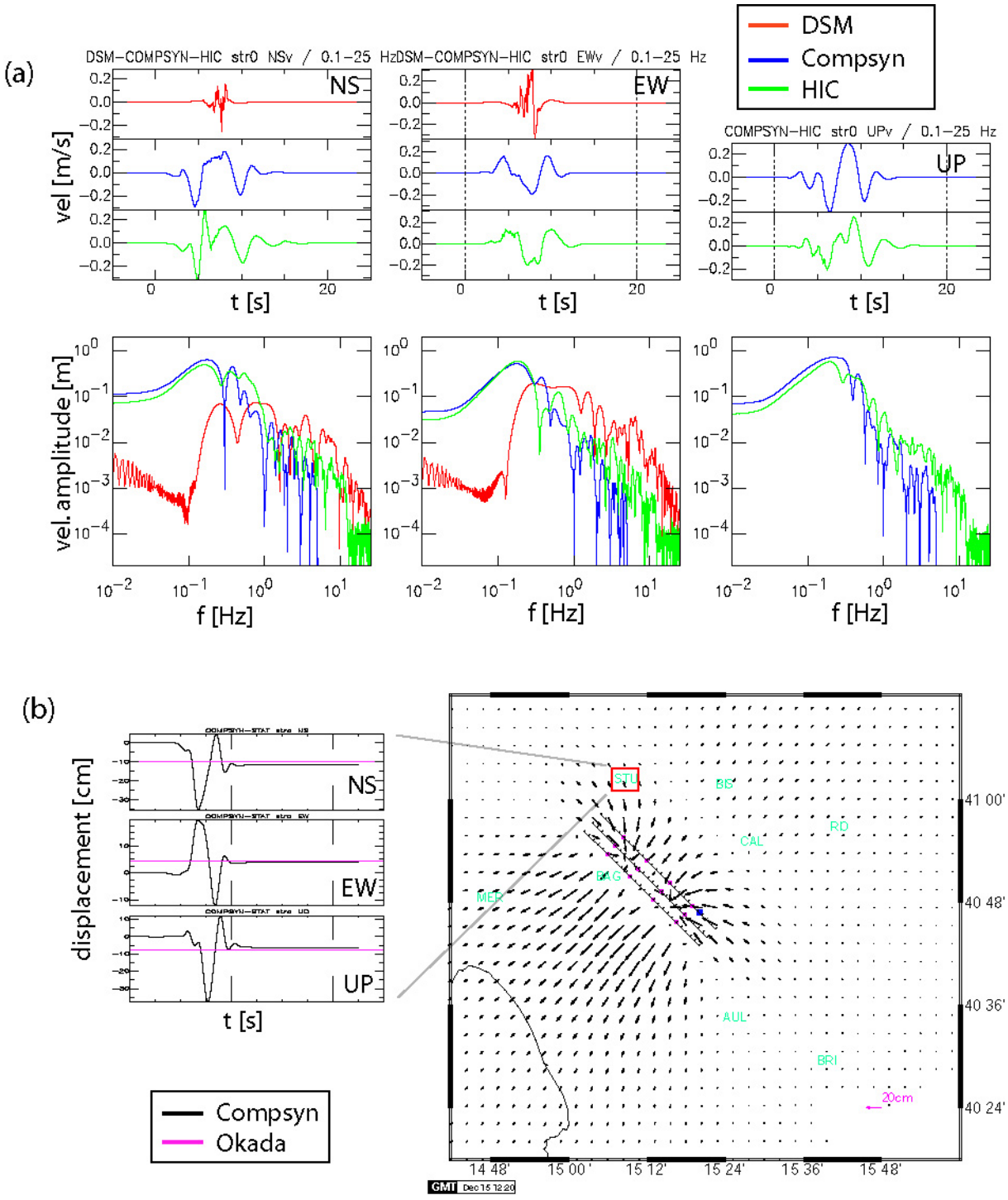

Figure 3.6.1 Same caption of Figure 3.1.1 but for Sturno (STU)

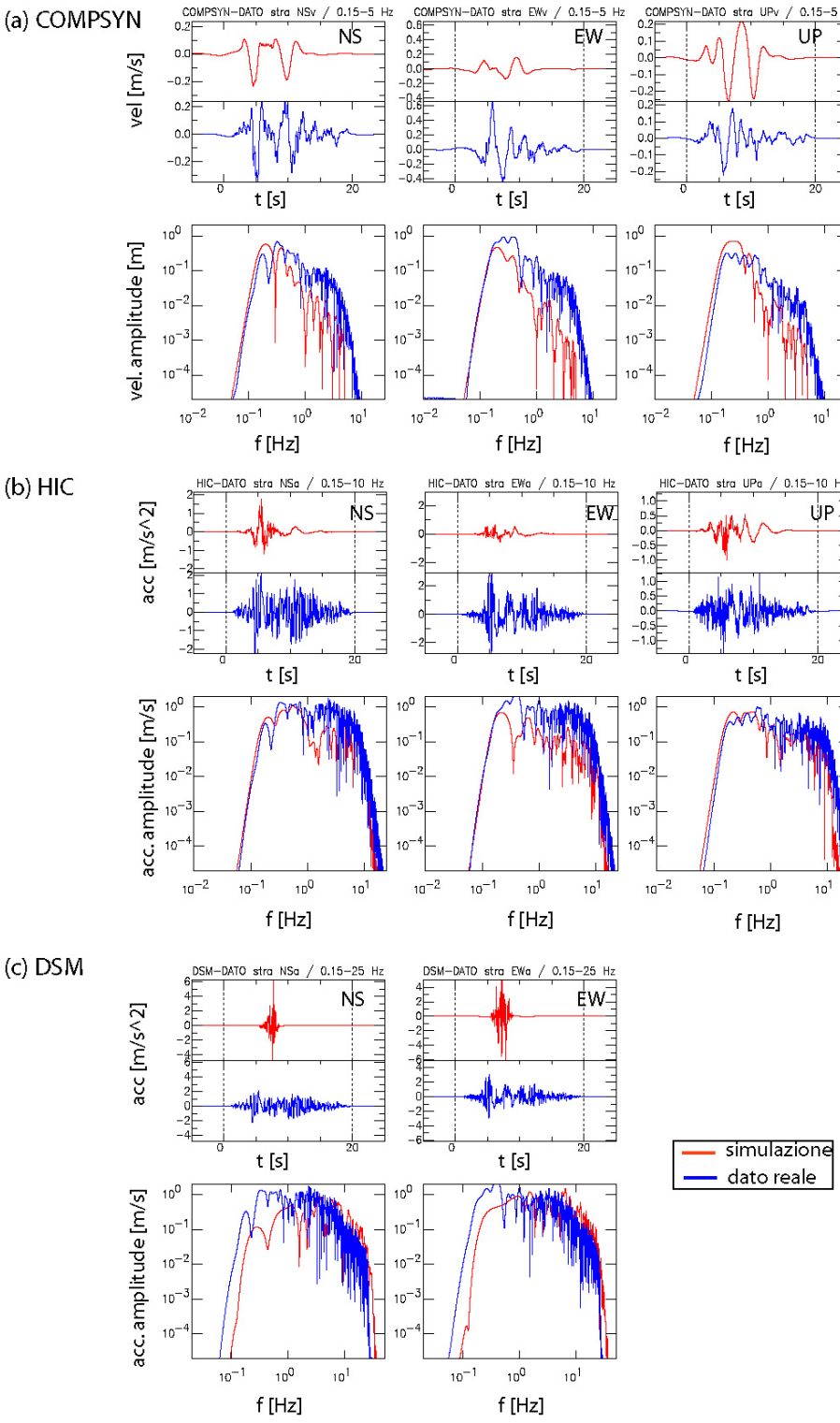

Figure 3.6.2. Same caption of Figure 3.1.2 but for STU

4. RESULTS

4.1. Scenarios results

We evaluated the ground motion from different rupture scenarios obtained by HIC and DSM techniques by varying the nucleation point, rupture velocity and slip distribution along the 0s Irpinia fault. In Table 4.1 are shown the model parameters, specifying those that remain fixed or change for the computation of different ground motion scenarios.

Table 4.1 – Kinematic model parameters for the two techniques

FIXED
1D propagation medium
Fault geometry and orientation
Focal mechanism
Seismic moment
Attenuation model

VARIABLE	HIC	DSM
Rupture velocity	1 (2.7 km/s)	3 (2.4; 2.7; 2.9 km/s)
Position of nucleation point	8 along the strike	3 along the strike
Final slip distribution	5	1
# Scenarios	**40**	**9**

Ground motion parameters are computed on a grid of receivers up to 100 km away from the source. In the following figures we present some peak acceleration and velocity maps and we analyze how the ground motion distribution depends on the variable parameters illustrated above.
We first compared the PGV maps computed with the two simulation techniques, considering the fixed location of the hypocenter and a fixed rupture velocity of 2.7 km/s (Figure 4.1). The PGV maps from the two simulation techniques are very similar and they show the effect of directivity on the intermediate frequency range.

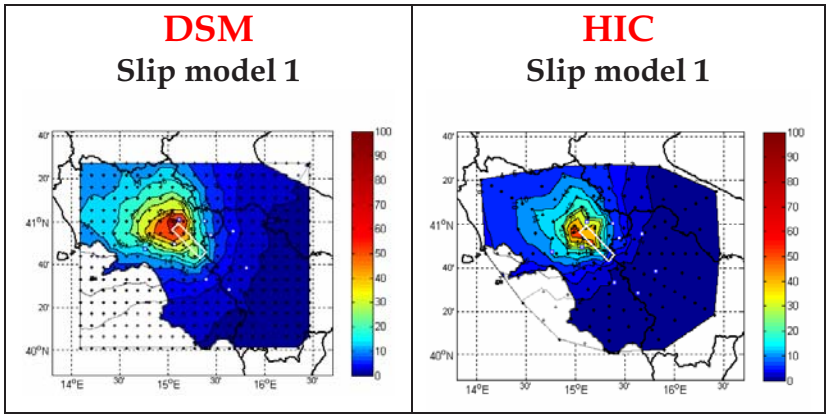

Figure 4.1 – PGV maps computed with DSM (left) an Hic (right) techniques for the same rupture model (slip model 1, rupture velocity=2.7 km/s).

We then analyzed the variation of ground motion parameters on slip and velocity models. In figure 4.2 are shown the PGA maps obtained varying the rupture velocity while position of nucleation point (center of the fault) and slip distribution are fixed. As we can see peak values increase as rupture velocity increases from 2.4 to 2.9 km/s.

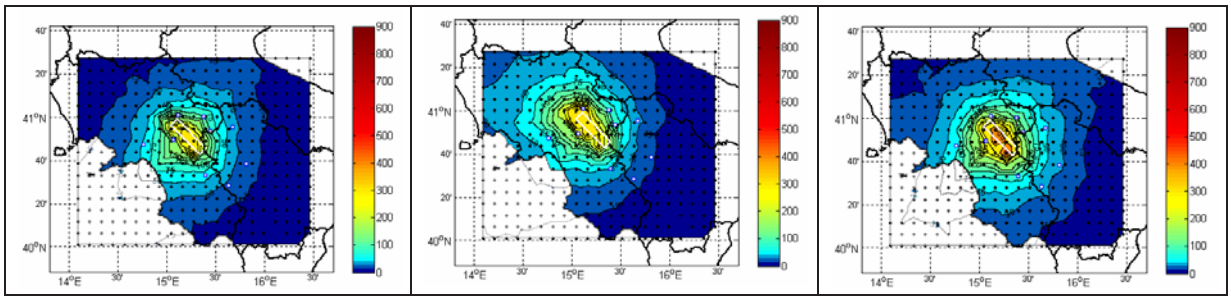

Figure 4.2 - PGA maps computed with DSM techniques considering different rupture velocity (from left, 2.4, 2.7 and 2.9 km/s).

In Figure 4.3 and 4.4 we fixed the slip distribution and rupture velocity and we change the position of the nucleation in order to obtained a different rupture propagation on the fault surface. DSM maps (Figure 4.3) show clear directivity effects and the area of maximum shaking moves according to the position of the nucleation point. These effects are less evident in HIC simulations presented in figure 4.4.

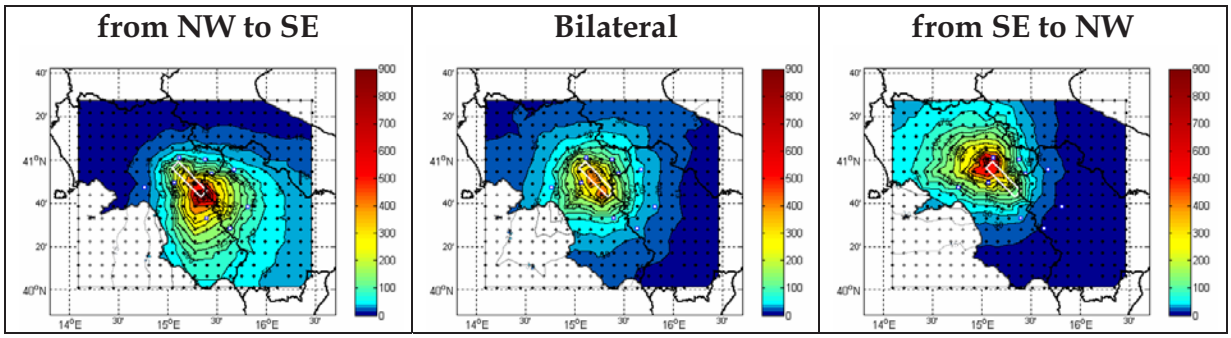

Figure 4.3 - PGA maps computed with DSM technique considering different position of the nucleation point (rupture velocity = 2.9 km/s).

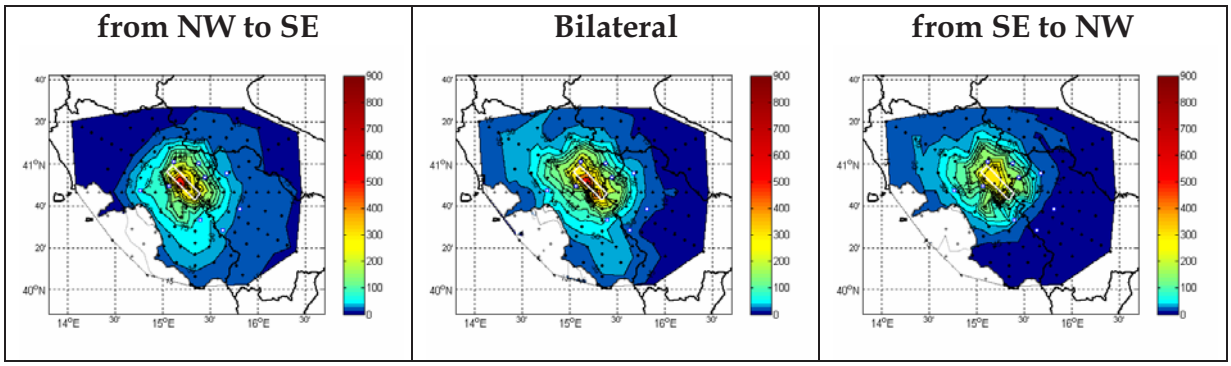

Figure 4.4 - PGA maps computed with HIC technique considering different position of the nucleation point (rupture velocity = 2.9 km/s).

Figure 4.5 shows a comparison between PGV maps computed with the two simulation techniques. In these cases we considered a fixed location of the hypocenter and a fixed rupture velocity (2.7 km/s), varying the slip distribution on the fault in HIC simulation model. Considering three different k-squared slip models among the five hypothesized we can see how the HIC PGV maps depend on slip distribution. Furthermore the maximum values varying in accordance to asperity position.

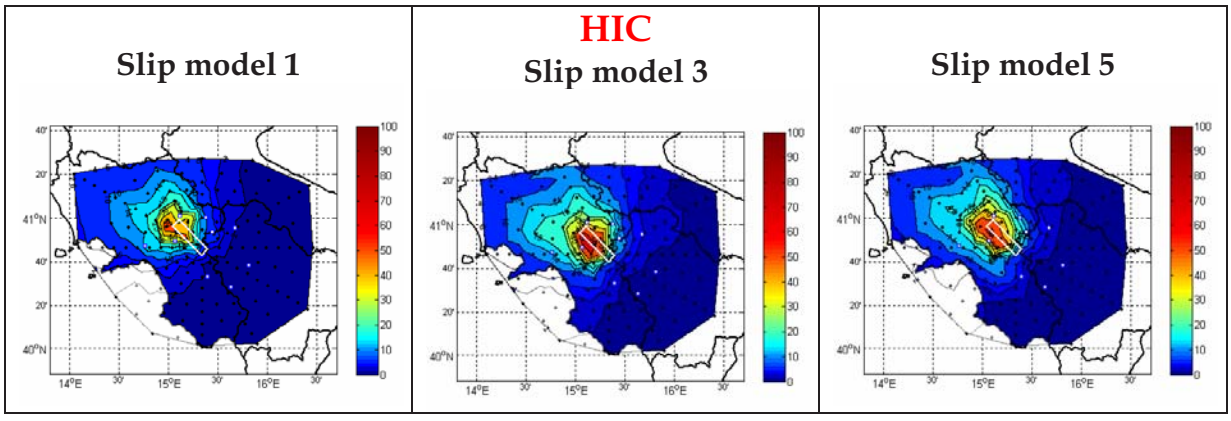

Figure 4.5 – PGV maps computed with DSM (top) an Hic (bottom) techniques considering different K^2 slip model.

4.2. Comparison with empirical attenuation relationships

Empirical attenuation relationships provide strong motion estimates, for a given region, as a function of distance, magnitude and site condition. Fault geometry is taken into account by using the distance from the surface projection of the fault (Rjb) instead of the epicentral distance. We used the Sabetta and Pugliese (*1996;* **SP96**) and the Ambraseys et al. (*2005,* **AMB05**) relationships, developed for Italian and European territory, respectively, to compare the synthetic scenarios computed for the 0s Irpinia fault using DSM and HIC methods.

We decided to represent the scenarios results with a fit curve (fig. 4.5) as a function of the R_{jb} (for each site the R_{jb} is computed with respect to the 0s fault geometry). To calculate this curve we divided the R_{jb} distance in bins (e.g. 0< R_{jb} <4 km) and, for each interval we computed the mean and standard deviation of the peak values. The bin's dimensions increase with R_{jb}. Furthermore we plot the peak values recorded on rock site and soil site during the Irpinia earthquake.
The mean PGA values obtained from DSM and HIC are very similar; DSM standard deviation is higher than the one from HIC, as in DSM the more pronounced directivity effects introduce a large variability. The two techniques present very similar results also in terms of mean PGV values, but HIC standard deviation is higher than that from DSM, especially at short distances, as in HIC the sensitivity to the slip model introduces more variability. The PGA and PGV recorded at rock site are well fitted by the average curves computed from simulations.

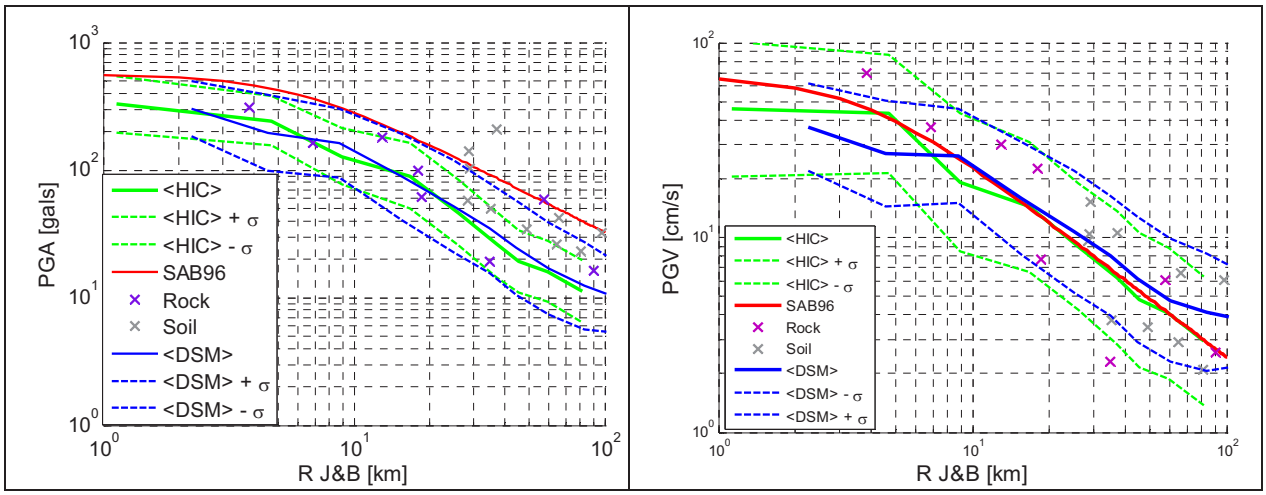

Figure 4.5. Average PGA (left panel) and PGV (right panel) curves from DSM and HIC simulations compared with SP96 as a function of R_{jb}.. Crosses represent recorded data from the 1980 event.

In figure 4.6 we compare synthetic PGA computed with DSM technique for bilateral and unilateral rupture processes and for 3 different rupture velocities with empirical attenuation laws. In figure 4.6d the simulated peaks from the all shaking scenarios are averaged using a log-normal distribution. The synthetic mean values are lower than ones predicted by the SP96 and AMB05, and their standard deviation is large.

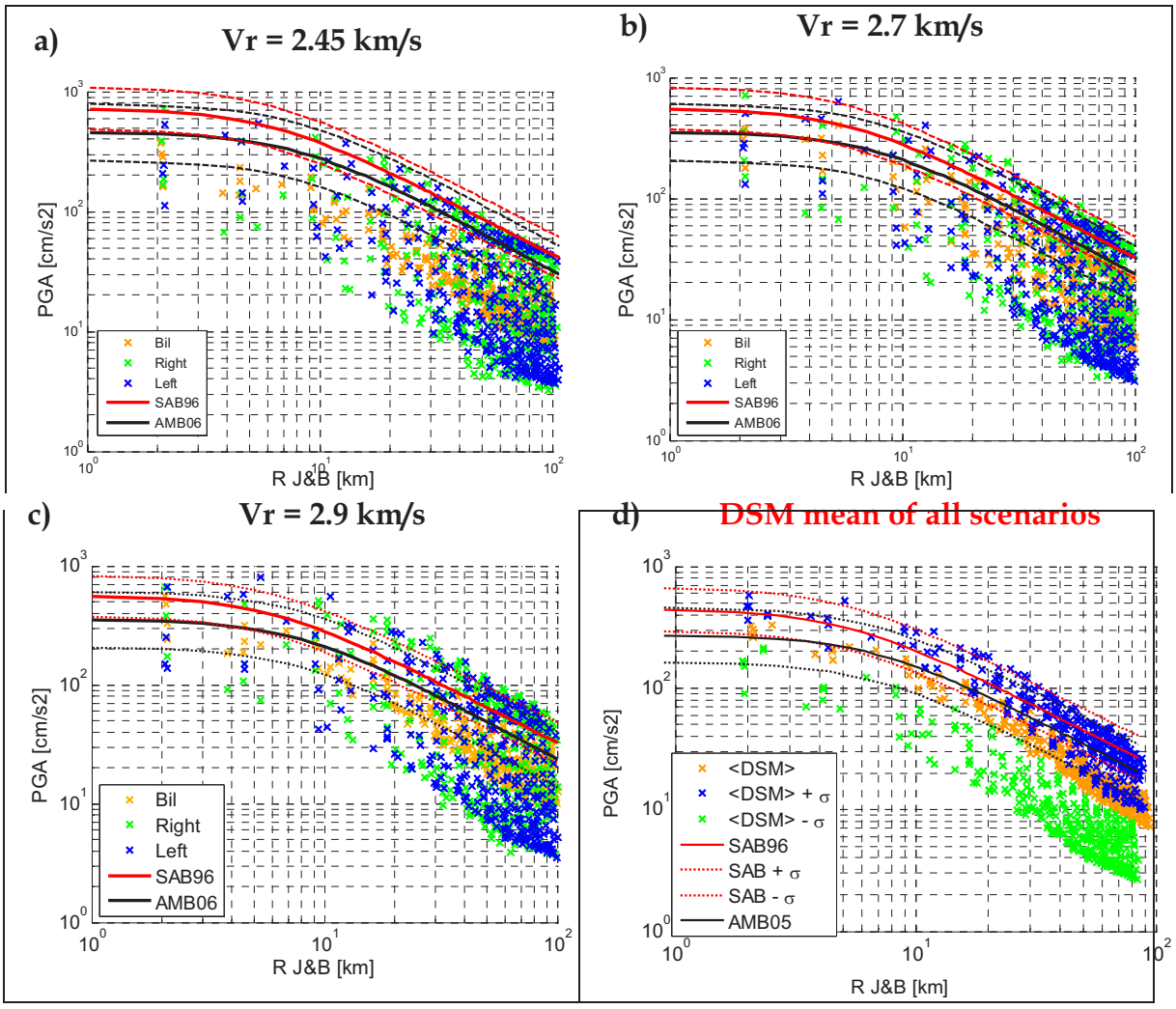

Figure 4.6 – Comparison between PGA values computed with DSM technique and empirical attenuation laws (AMB05 and SP96) as a function of R_{jb}. a) rupture velocity 2.45 km/s and 3 different nucleation points. b) rupture velocity 2.7 km/s and 3 different nucleation points. c) rupture velocity 2.9 km/s and 3 different nucleation points. d) mean ± 1 standard deviation considering all hypothesized scenarios.

In Figure 4.7 we compare synthetic PGV, obtained by HIC simulation technique, with SP96 attenuation law. Figure 4.7a shows PGV computed considering 1 fixed hypocenter location and 3 possible slip distributions. In figure 4.7b we fixed the slip model and we choose 3 possible position of the nucleation point among the 8 considered in the HIC simulation model. Figure 4.7c shows the overall variability of PGV as a function of R_{jb} considering all possible scenarios (5 slip models and 8 hypocenter locations). In figure 4.7d the simulated peaks from the all shaking scenarios are averaged using a log-normal distribution. The synthetic mean values are equal to ones predicted by the SP96 law, while the synthetic standard deviation is large.

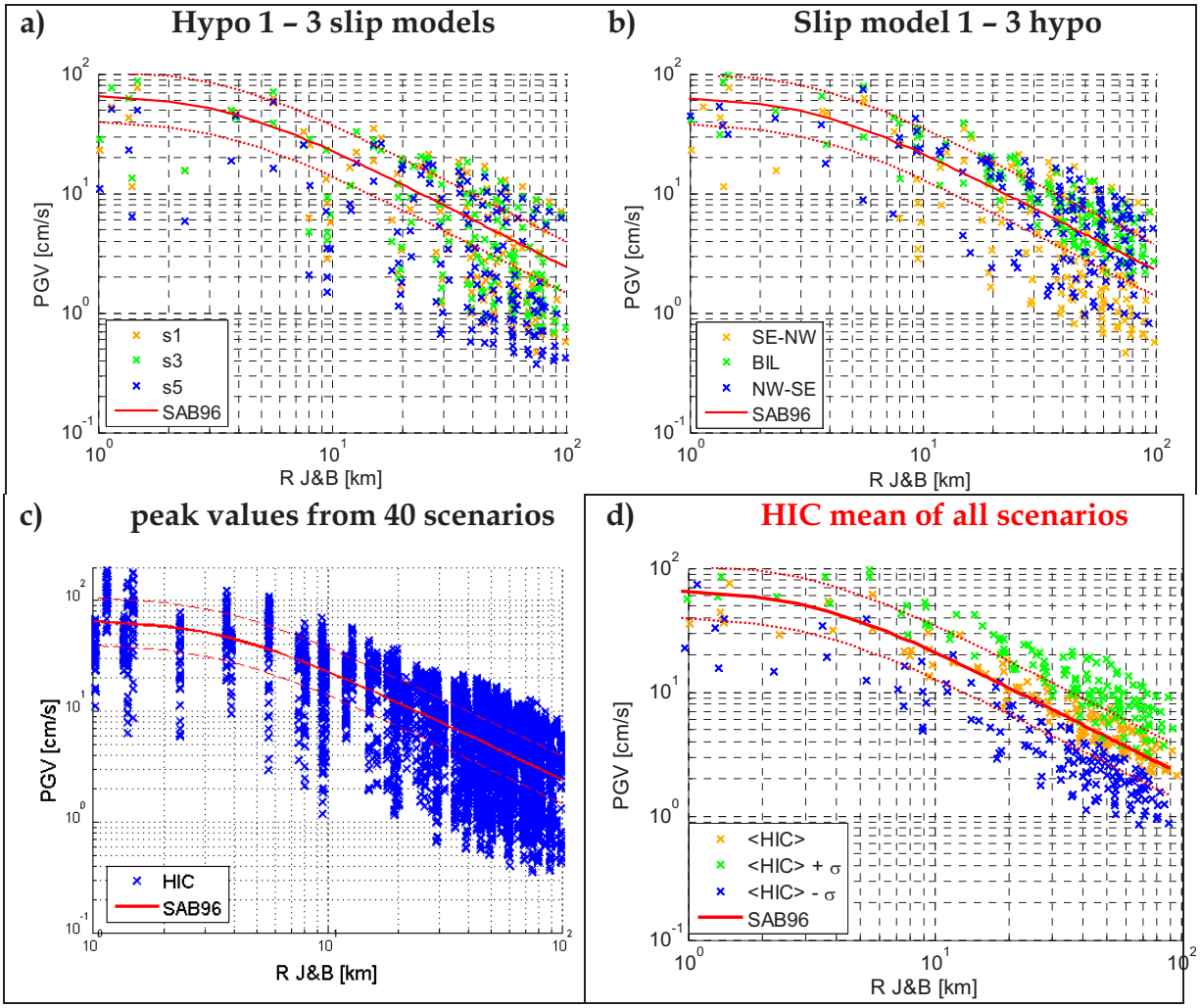

Figure 4.7 - Comparison between PGV values computed with HIC technique and empirical attenuation law (SP96) as a function of R_{jb}. a) assuming 1 hypocenter position and 3 different slip models. b) assuming 1 slip model and 3 different hypocenter positions. c) considering all possible scheme of hypocenter location and slip distribution. d) mean ± 1 standard deviation considering all hypothesized scenarios.

REFERENCES

AKI, K. (1967), Scaling Law of Seismic Spectrum, J. Geophys. Res. 72, 1217–1231.

Amato, A., Selvaggi, G., 1993. Aftershock location and P-velocity structure in the epicentral region of the 1980 Irpinia earthquake.Ann. Geofis. 36, 3– 15.

Ambraseys, N.N., Douglas, J., Sarma, S.K., Smit, P.M., Equations for the estimation of strong ground motions from shallow crustal eathquakes using data from Europe and Middle East: Horizontal peak ground acceleration and spectral acceleration, *Bull. of earthquake engineering*, **3**, 1-53, 2005.

Andrews D.J. , A stochastic fault model: 1. static case, *J. Geophys. Res.* **85**, 3867-3877, 1980.

BERESNEV, I. A. and ATKINSON, G. M. (1997), Modeling Finite-fault Radiation from the xn Spectrum, Bull. Seismol. Soc. Am. 87, 67–84.

BERESNEV, I. A. and ATKINSON, G. M. (1998a), FINSIM—a FORTRAN Program for Simulating Stochastic Acceleration Time Histories from Finite Faults, Seism. Res. Lett. 69, 27–32.

BERESNEV, I. A. and ATKINSON, G. M. (1998b), Stochastic Finite-fault Modeling of Ground Motions from the 1994 Northridge, California Earthquake. I. Validation on Rock Sites, Bull. Seismol. Soc. Am. 88, 1392–1401.

Bernard P., and A. Zollo, The Irpinia (Italy) 1980 earthquake: detailed analysis of a complex normal faulting, *J. Geophys. Res.* **94**, 1631-1647, 1989.

Boore, D.M., [1983] "Stochastic simulation of high-frequency ground motions based on seismological model of the radiated spectra," *Bull. Seism. Soc. Am.*, 73, pp. 1865-1894.

Boore, D.M. [2003] "Simulation of ground motion using the stochastic method," *Pure Appl. Geophys*. 160, pp. 635-676.

Bouchon, Michel (1981) A simple method to calculate Green's functions for elastic layered media , *Bull. Seism. Soc. Am.*, 71, 959-971

BRUNE, J. N. (1970), Tectonic Stress and the Spectra of Seismic Shear Waves from Earthquakes, J. Geophys. Res. 75, 4997–5009.

BRUNE, J. N. (1971), Correction, J. geophys. Res. 76, 5002.

Cocco, M. and F. Pacor. The rupture process of the 1980 Irpinia, Italy, earthquake from the inversion of strong motion waveforms, *Tectonophysics*, **218**, 157-177, 1993.

Day, S.M., 2001. Test of 3D elastodynamics codes, Final Report to the Pacific Earthquake Engineering Research Center , Lifeline Program Task 1A01, sept. 10, 2001

Gallovic, F., Brokešová, J. (2004). On strong ground motion synthesis with k^-2 slip distributions, J. Seismology 8, 211-224.

Gallovic, F. and J. Brokesova, Hybrid k-squared Source model for strong motion simulations: an introduction (submitted to *PEPI*) 2006.

Heaton, T. (1990). Evidence for and implications of self-healing pulses of slip in earthquake rupture. *Phys. Earth Plane. Interiors* 64, 1-20.

Herrero A. And Bernard (1994)

Improta L., Bonagura M., Capuano P., Iannaccone G., An integrated geophysical investigation of the upper crust in the epicentral area of the 1980, M_s=6.9, Irpinia earthquake (Southern Italy). Tectonophysics 361 (2003) 139-169.

Motazedian, D. and G. Atkinson (2005). Stochastic finite-fault model based on dynamic corner frequency. *Bull. Seism. Soc. Am.* 95, 995-1010.

Okada Y., 1985 Surface deformation due to shear and tensile faults in a half-space, *Bull. seism. Soc. Am.*, **139**, 1135–1154.

Olson, A.H., Orcutt, J.A., and Frazier, G.A., 1984, The discrete wavenumber / finite element method for synthetic seismograms, Geophys. J.R. Astr. Soc.,v.77,421-460.

Pacor, F., Cultrera, G., Mendez, A. , Cocco, M. [2005]. "Finite Fault Modeling of Strong Ground Motion Using a Hybrid Deterministic - Stochastic Method," *Bull. Seism. Soc. Am.*, 95, 225-240.

Sabetta, F. and A. Pugliese, Estimation of response spectra and simulation of non-stationary earthquake ground motions, *Bull. Seism. Soc. Am.*, **86**, 337-352, 1996.

Selvaggi G., Amato A. (1993): Aftershock location and P-velocity structure in the epicentral region of the 1980 Irpinia earthquake, *Annali di Geofisica*, **36**, 3-15.

Spudich, P., and Archuleta, R, 1987, Techniques for earthquake ground motion calculation with applications to source parameterisation of finite faults, in Bolt, B.A. ed., SEISMIC STRONG MOTION SYNTHETICS: Orlando, Florida, Academic Press, p.205-265.

Spudich, P., Xu, L., Documentation of software package Compsyn sxv3.11: programs for earthquake ground motion calculation using complete 1-d green's functions, *International Handbook of Earthquake and Engineering Seismology CD, Int. Ass. Of Seismology and Physics of Earth's Interior, Academic Press, 2002.*

Spudich, P., Frazer, N.L. [1984] "Use of ray theory to calculate high-frequency radiation from earthquake sources having spatially variable rupture velocity and stress drop," *Bull. Seismol. Soc. Am.*, 74, pp. 2061-2082.

Steketee, J.A. (1958). On Volterra' dislocation in a semi-infinite elastic medium, Can. J. Phys. 36, 192,205.

Valensise, G., A. Amato, L. Beranzoli, E. Boschi, M. Cocco, D. Giardini and D. Pantosti, (1989). Un modello di sintesi del terremoto Campano-Lucano del 23 Novembre 1980, Atti 8° Convegno G.N.G.T.S., Rome, 1989.

Westaway, R., and J. Jackson (1984). Surface faulting in the southern Italian Campania-Basilicata earthquake of 23 November 1980, *Nature*, **312**, 436-438.

ZENG, Y. H., ANDERSON, J. G., and YU, G. A. (1994), Composite Source Model for Computing Realistic Synthetic Strong Ground Motions, Geophys. Res. Lett. 21, 725–728.